上海交通大学学位论文

稀有衰变实验氡及氡子体的控制

姓　　名：吴粮宇

学　　号：520072910021

导　　师：孟月

学　　院：物理与天文学院

专业名称：物理学

申请学位层次：学士

2024 年 06 月

A Dissertation Submitted to

Shanghai Jiao Tong University for Bachelor's Degree

CONTROL OF RADON AND RADON DAUGHTERS IN RARE DECAY EXPERIMENTS

Author: Liangyu Wu

Supervisor: Yue Meng

School of Physics and Astronomy

Shanghai Jiao Tong University

Shanghai, P.R. China

June, 2024

上海交通大学

学位论文原创性声明

本人郑重声明：所呈交的学位论文，是本人在导师的指导下，独立进行研究工作所取得的成果。除文中已经注明引用的内容外，本论文不包含任何其他个人或集体已经发表或撰写过的作品成果。对本文的研究做出重要贡献的个人和集体，均已在文中以明确方式标明。本人完全知晓本声明的法律后果由本人承担。

学位论文作者签名：吴粮宇

日期：2024年06月03日

上海交通大学

学位论文使用授权书

本人同意学校保留并向国家有关部门或机构送交论文的复印件和电子版，允许论文被查阅和借阅。

本学位论文属于：

☑**公开论文**

☐**内部论文**，保密☐1年/☐2年/☐3年，过保密期后适用本授权书。

☐**秘密论文**，保密____年（不超过10年），过保密期后适用本授权书。

☐**机密论文**，保密____年（不超过20年），过保密期后适用本授权书。

（请在以上方框内选择打“✓”）

学位论文作者签名：吴粮宇　　指导教师签名：孟用

日期：2024年06月03日　　日期：2024年06月03日

摘 要

暗物质和中微子的研究代表了目前粒子物理学中最有可能率先发现新物理的两个突破口。对于前者，物理学家们至今还不了解其具体属性和相互作用方式。相应地，世界上有一批实验在力求搜寻到不同暗物质模型存在的信号。相较暗物质而言，中微子的相关理论更为完善一些，但仍有如中微子振荡参数的测量和无中微子双贝塔衰变等一系列问题在等待着人们的研究。由于无论是暗物质还是中微子，它们与普通物质发生相互作用的截面都极小，因此此类稀有事例探测实验通常对于实验环境和辐射本底的要求极为严苛。在此类实验中，实验物理学家们不仅需要极力提升探测器的灵敏度，更要想办法降低实验的本底水平，以求清晰地分辨出目标事例。

本文首先介绍了有关暗物质和中微子的一些物理图像和研究历史，并展示了相关领域内目前正在运行或即将开展的几个代表性实验。随后，本文介绍了关于低本底实验中氡及氡子体的来源以及对于实验的影响原理。氡是目前不同实验探测器中的一种共同的主要放射性本底。为了降低实验中的氡本底，或是更好地了解实验中残存的氡本底信息，实验物理学家们研发出了一系列关于氡及氡子体的控制和测量系统。此外，由于低本底实验中膜类材料的广泛使用，我们需要更好地了解不同膜材料的氡气阻挡效果。本文详细介绍了氡扩散腔体的设计和实验步骤，并展示了实验中常用到的四种膜材料的氡扩散系数的测量结果。最后，本文提出了几个未来有可能用于控制或测量低本底实验中氡本底的方法，希望可以为未来稀有事例探测实验的氡本底控制带来一些有意义的参考思路。

关键词：稀有事例探测，暗物质，中微子，氡

ABSTRACT

Research on dark matter and neutrinos represents two of the most promising avenues for discovering new physics in particle physics today. Regarding the former, physicists remain uncertain about its specific properties and interactions. Consequently, many experiments worldwide are striving to detect signals from different dark matter models. In contrast to dark matter, the theoretical framework for neutrinos is more established, yet issues such as the measurement of neutrino oscillation parameters and neutrinoless double-beta decay still require further investigation. Because both dark matter and neutrinos interact very weakly with ordinary matter, rare event detection experiments often have extremely stringent requirements for the experimental environment and background radiation. Experimental physicists must not only enhance the sensitivity of detectors but also find ways to reduce background noise to identify target events clearly.

This thesis first introduces the physical concepts and research history of dark matter and neutrinos and presents several representative ongoing or upcoming experiments in these fields. It then explores the sources of radon and its progeny in low background experiments and explains how they affect the experiments. Radon is a major common radioactive background in various detectors. Experimental physicists have developed a series of control and measurement systems for radon and its progeny to reduce radon background or better understand residual radon levels in experiments. Additionally, due to the widespread use of membrane materials in low background experiments, it is crucial to understand the radon-blocking effect of membrane materials. This thesis provides a detailed description of the design and experimental procedure of the radon diffusion chamber and presents the measurement results of the radon diffusion coefficients for four commonly used membrane materials. Finally, the thesis proposes several future strategies and methods for controlling or measuring radon background in low background experiments, offering valuable insights for future rare event detection experiments.

Key words: rare event detection, dark matter, neutrino, radon

Contents

List of Figures

List of Tables

Chapter 1 Introduction to Dark Matter and Neutrinos

Particle physics tries to uncover the fundamental mysteries of the universe and help us better understand this fantastic world. The establishment of the Standard Model (SM) of particle physics[1] has provided us with a theory that can describe the interactions between all known fundamental particles, excluding gravitational interactions. On July 4, 2012, high-energy physicists at CERN's Large Hadron Collider (LHC) announced the discovery of the Higgs boson at 126 GeV/c^2. With this discovery, all the elementary particles in the Standard Model, as shown in Figure 1–1, have been found. However, physicists have increasingly discovered results that go beyond the predictions of the Standard Model, among which some may be answered by a category of experiments known as rare decay experiments.

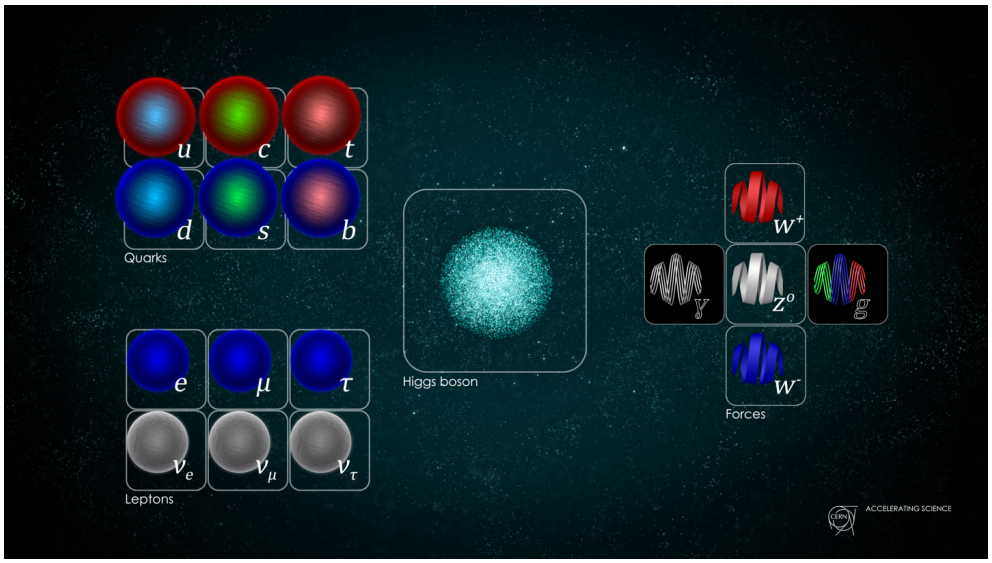

Figure 1–1 Particles of the Standard Model of particle physics. Taken from[2]

Rare decay experiments represent a cutting-edge topic in particle and nuclear physics, where measurements of atomic decay processes with extremely small reaction cross-sections or very long half-lives are referred to as rare event detection[3]. In recent years, hot topics such as the detection of dark matter (DM), the measurement of neutrinoless double-beta decay (NLDBD), and the measurement of neutrino properties have been pursued. These experiments are usually extremely challenging, as the infrequent detection events are often

drowned out by a large amount of background noise, requiring unusually clean experimental environments and highly sensitive detectors. This chapter will first introduce some basic information and related research history regarding rare event detection experiments' frequent guests: dark matter and neutrinos.

1.1 Dark Matter

Dark matter gets this cool name because it neither emits nor absorbs light. Although all kinds of theories and experiments about dark matter exist, we know very little about it because it rarely interacts with ordinary matter in strong or electromagnetic forces. However, dark matter does matter. Compelling astronomical evidence shows that ordinary matter, as described by the Standard Model, only makes up 5% of our universe. The rest is composed of 27% dark matter and 68% dark energy[4]. Therefore, although the task of discovering dark matter is challenging, scientists must find and understand it, which is essential for understanding the composition of matter and the evolution of our universe.

1.1.1 The Evidence for Dark Matter

The research about dark matter can be traced back to the astronomical observations by Fritz Zwicky in 1933. In his studies of the velocity of galaxies in the Coma Cluster, he discovered that the cluster contained a significant amount of mass that did not emit radiation. According to Newton's law of universal gravitation, if we measure the tangential velocity v of visible stars on the disk of a galaxy as a function of their distance from the galaxy's center r, we would expect that the velocity of stars farther from the core would decrease following a $1/\sqrt{r}$ relationship. However, a significant discrepancy was found when comparing theoretical calculations with observational data.

In 1959, Louise Volders discovered in the study of the rotation curve of the M-33 galaxy that the velocity of stars far from the galaxy center significantly increased[5], deviating from what was expected by kinematic laws (see Figure 1–2). Vera Rubin later discovered the flat galactic rotation curves in ten spiral galaxies[6], which is crucial because it implies that, unless we are willing to fundamentally challenge Newton's laws and general relativity at specific scales, we must acknowledge that most of the mass in galaxies is non-luminous, i.e., dark matter. In other words, a vast amount of dark matter is distributed in a spherical halo,

within which visible galaxies are situated.

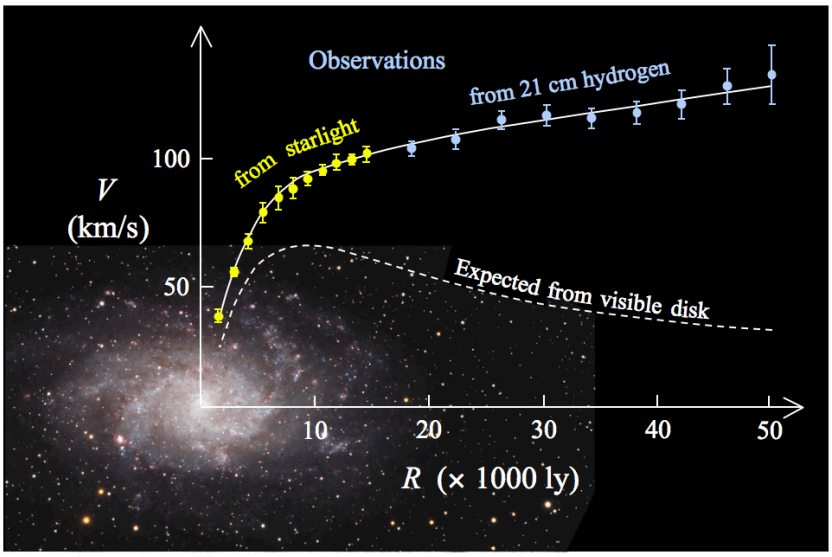

Figure 1–2 Rotation curve of M-33 galaxy. Taken from[5]

The evidence from the other side comes from measurements of the Cosmic Microwave Background (CMB) radiation. The CMB radiation is a gravitationally red-shifted radiation from ancient photons originating from the early universe that have remained over time. Since the shape of the radiation power spectrum is determined by the oscillations of the early universe's hot gases, identifying the resonance frequencies and amplitudes of these oscillations can help provide information related to the composition of cosmic matter. Moreover, CMB's angular power spectrum measurements match very well with the ΛCDM (Lambda cold dark matter) model in the Standard Model of cosmology. According to data from PLANCK[4,7], ordinary baryonic matter constitutes only about 5% of the universe, while dark matter accounts for nearly 27%.

Moreover, the existence of dark matter theory can also explain the phenomenon of the Bullet Cluster, which is one of the most direct pieces of evidence for the existence of dark matter because the dark matter evidence from this observation does not rely on Newtonian mechanics. When two clusters of galaxies collide at high speeds, the cross-section for scattering between ordinary matter is much larger than that between dark matter, so the ordinary matter quickly loses kinetic energy after the collision and remains near the collision point. However, dark matter does not slow down like those particles. Still, it is propelled by the immense energy generated by the merging of the galaxy clusters, passing through the center

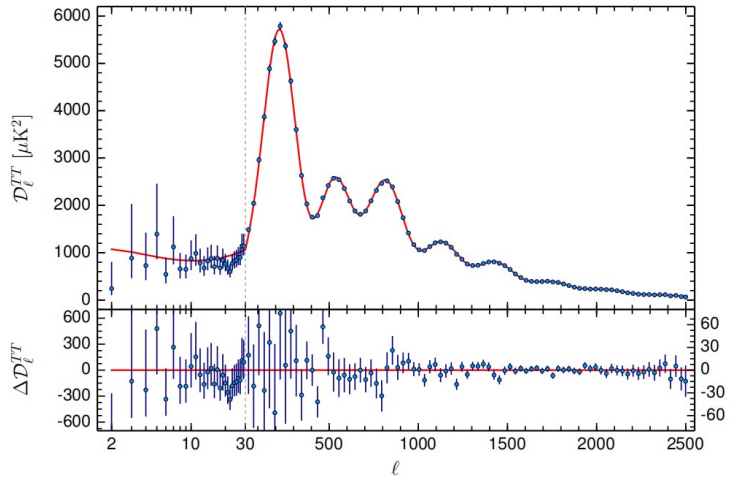

Figure 1–3 The Planck 2015 CMB power spectrum. The upper panel shows the ΛCDM model's spectrum, best matched to Planck TT+lowP data. Taken from[7]

and emerging at the ends of the nebula, causing a separation of ordinary luminous matter and dark matter. The gravitational lensing effect can calculate the total mass distribution of the galaxy cluster, and detectors near Earth (such as the Chandra X-ray telescope) can provide the mass of luminous celestial bodies, thus the existence of dark matter can be explained by the difference between the two. The result that most of the clusters passed through each other unperturbed suggests once again that the majority of the clusters are dark matter.

1.1.2 Dark Matter Candidates

To date, we know very little about the properties of dark matter, but some information is certain. First, dark matter particles must be non-baryonic particles, meaning they do not participate in strong interactions. Moreover, dark matter does not interact electromagnetically with ordinary matter but must interact gravitationally with it. Also, dark matter particles may have been abundantly present from the early stages of the universe's formation, and they should be relatively stable and not prone to decay. In the SM, only neutrinos might fulfill the requirements to be regarded as dark matter. Still, given the constraints on the density of neutrinos in the universe, even if neutrinos are dark matter, they can only account for a tiny fraction of the total amount. Therefore, we must look beyond the SM to find suitable dark matter particle candidates[8]. The following content will introduce some of the most compelling candidates.

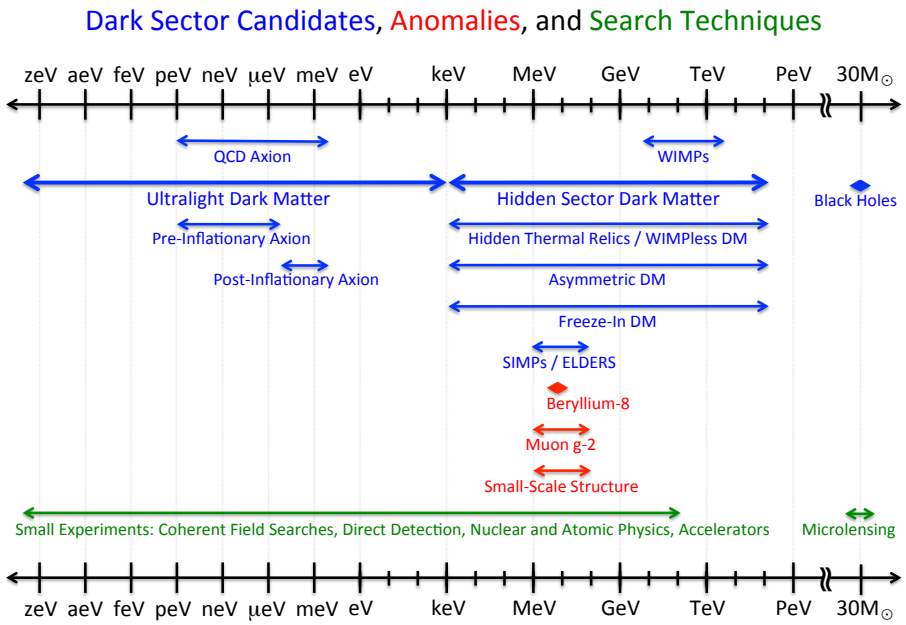

Figure 1–4 Dark matter candidates in different mass ranges and some of the search techniques. Taken from[9]

Supersymmetry theory[10] is a unified theory that extends the symmetry of the SM to incorporate all four fundamental forces of nature. It posits that every elementary particle in the SM has a supersymmetric partner whose spin differs by 1/2 from its own. In numerous supersymmetry models, such as the Minimal Supersymmetric Standard Model (MSSM)[11], the parity between SM particles and their supersymmetric counterparts must be conserved. This leads to the production of supersymmetric particles in pairs, with heavier supersymmetric particles decaying into lighter ones, where the Lightest Supersymmetric Particle (LSP) is expected to be stable. Within these models, the LSP has a residual amount that can explain the abundance of dark matter in the universe, and its mass range, from GeV to TeV, also makes it a highly competitive dark matter candidate. Since these particles interact with SM particles only through gravity and another weak force, similar in strength to the weak nuclear force, they are commonly referred to as Weakly Interacting Massive Particles (WIMPs)[12].

WIMPs have long been considered the most favored theoretical candidates for dark matter, mainly due to the "WIMP miracle", a serendipitous alignment between particle theory, particle experiment, and cosmology. If WIMPs are stable and exist, they naturally explain the current abundance of dark matter in the universe. The production of dark matter as ther-

mal relics from the Big Bang enables us to predict that a particle responsible for all dark matter would typically have a mass of 100 GeV to 1 TeV[13]. Such weak-scale particles feature order-one couplings and achieve the correct freeze-out conditions to match the observed relic density. Moreover, this scenario is consistent with various predictions that extend beyond the standard model of particle physics, shedding light on the potential characteristics of dark matter particles. This miracle indicates that many particle physics models could offer suitable dark matter candidates. The theoretical elegance and high feasibility make WIMPs an outstanding candidate for dark matter.

In addressing the strong CP violation problem, physicists introduced a new low-mass neutral boson, the axion[14-15]. In this theory, a vast and stable population of axions in the universe could well explain the components of dark matter. The characteristic that axions can convert into photons in strong magnetic fields is often used as the primary experimental approach for axion detection. However, even if observed, they could only explain a small portion of dark matter, much like ordinary neutrinos, rather than its entirety due to the low density of axons.

Yet, another type of neutrino with sufficient mass could fulfill this role, known as sterile neutrinos. The neutrinos commonly observed in experiments are left-handed, but according to grand unified theory models[16], neutrinos should adhere to the See-Saw mechanism, suggesting the possibility of the existence of heavy right-handed neutrinos whose masses are inversely proportional to those of the ordinary left-handed neutrinos[17]. Sterile neutrinos would interact with SM particles only through weak interaction and gravity. Since they would mix with ordinary neutrinos, theoretically, if we could detect them indirectly, the dark matter in the universe might be identified.

1.2 Neutrinos

To explain the seeming energy conservation law-violating continuous beta decay spectrum, Wolfgang Pauli proposed the existence of a very light, electrically neutral particle that carries away the missing energy. This particle was later renamed “neutrino” by Enrico Fermi. Thus, the complete beta decay process is represented by Equation 1–1.

$$n \longrightarrow p^{+} + e^{-} + \bar{\nu} \tag{1–1}$$

However, due to the neutrino's extremely weak interaction with matter, people were skeptical of its existence, considering it a hypothetical particle invented to save the conservation laws until the 1950s. It wasn't until 1956 that Clyde Cowan and Frederick Reines built a large water tank to observe neutrinos from a reactor undergoing inverse beta decay (as shown in Equation 1–2). They used water with dissolved $CdCl_2$ (40 kg per hundred liters) as the target material, where the water tanks were sandwiched between three scintillator layers composed of many photomultiplier tubes (PMT). By capturing the signals of the produced positrons and neutrons, the existence of neutrinos was finally directly proven[18-19].

$$\bar{\nu}_e + p^+ \longrightarrow e^+ + n \tag{1–2}$$

Later, physicists discovered specific reactions that seemed not to be forbidden yet were never observed, such as Equation 1–3. Subsequently, muon neutrinos[20] and tau neutrinos[21] were found. However, research on neutrinos extends far beyond these findings, with many more questions about this tiny particle being raised over time.

$$\mu^- \nrightarrow e^- + \gamma \tag{1–3}$$

1.2.1 Neutrino Oscillation

This story should begin with humanity's never-ending exploration of the sun. To fully understand the conditions inside the sun, we need to identify which physical processes are taking place on it. The characteristic of neutrinos that makes them almost unable to interact with matter allows them to easily pass through the sun and travel a long distance to reach Earth, making neutrinos the best probes for studying the sun's interior.

The first experiment to measure solar neutrinos occurred in a mine in South Dakota[22]. Ray Davis used a vast tank filled with chlorine and captured neutrinos through the reaction shown in Equation 1–4. However, after counting, he only obtained 1/3 of the number of neutrinos predicted by John Bahcall[23]. So here comes the famous solar neutrino problem: Why did the remaining neutrinos disappear?

$$\nu_e + {}^{37}Cl \longrightarrow {}^{37}Ar + e^- \tag{1–4}$$

Bruno Pontecorvo proposed a physical explanation[24], which is the mechanism of neu-

trino oscillation known today. Neutrinos can spontaneously transform from one flavor to another during flight. This theory was later confirmed by experiments like Super-Kamiokande (SuperK) and the Sudbury Neutrino Observatory (SNO)[25-27].

The theory of neutrino oscillation indicates that neutrinos interact in flavor eigenstates (ν_e, ν_μ and ν_τ) but propagate in mass eigenstates (ν_1, ν_2 and ν_3). That is to say, flavor eigenstates are linear superpositions of these mass eigenstates, which mathematically can be represented with the help of the Pontecorvo–Maki–Nakagawa–Sakata (PMNS) matrix:

$$\begin{pmatrix} \nu_e \\ \nu_\mu \\ \nu_\tau \end{pmatrix} = \begin{pmatrix} U_{e1} & U_{e2} & U_{e3} \\ U_{\mu 1} & U_{\mu 2} & U_{\mu 3} \\ U_{\tau 1} & U_{\tau 2} & U_{\tau 3} \end{pmatrix} \begin{pmatrix} \nu_1 \\ \nu_2 \\ \nu_3 \end{pmatrix} \tag{1–5}$$

Similarly, this kind of mixing applies to quarks as well, but with a different matrix. In the case of neutrinos, each element of the PMNS matrix can be expressed by three mixing angles (θ_{12}, θ_{23} and θ_{13}) and one phase factor (δ):

$$U_{PMNS} = \begin{pmatrix} c_{12}c_{13} & s_{12}c_{13} & s_{13}e^{-i\delta} \\ -s_{12}c_{23} - c_{12}s_{23}s_{13}e^{i\delta} & c_{12}c_{23} - s_{12}s_{23}s_{13}e^{i\delta} & s_{23}c_{13} \\ s_{12}s_{23} - c_{12}c_{23}s_{13}e^{i\delta} & -c_{12}s_{23} - s_{12}c_{23}s_{13}e^{i\delta} & c_{23}c_{13} \end{pmatrix} \tag{1–6}$$

where $c_{ij} = cos\theta_{ij}$, $s_{ij} = sin\theta_{ij}$. Experimentally, we can determine these mixing angles with neutrinos from various sources. Data on θ_{12} is sourced from solar neutrinos and reactor antineutrinos, θ_{23} from atmospheric and accelerator neutrinos, and θ_{13} from reactor and accelerator neutrinos. We can get those values in the reference book[28].

$$\begin{aligned} sin^2\theta_{12} &= 0.307 \pm 0.017 \\ sin^2\theta_{23} &= 0.390 \pm 0.033 \\ sin^2\theta_{13} &= 0.0242 \pm 0.026 \end{aligned} \tag{1–7}$$

1.2.2 Neutrino Mass Hierarchy

The discovery of neutrino oscillations forces us to acknowledge a phenomenon beyond the SM, that is, neutrinos have mass, and their masses must be unequal. We know three mass

splittings for neutrinos today, as shown in Equation 1–8.

$$\begin{aligned} \Delta_{21} &= m_2^2 - m_1^2 \\ \Delta_{32} &= m_3^2 - m_2^2 \\ \Delta_{31} &= m_3^2 - m_1^2 \end{aligned} \tag{1–8}$$

Here, only two are independent ($\Delta_{31} = \Delta_{21} + \Delta_{32}$). Among these, one splitting is minor, while the others are significantly larger. Therefore, we naturally hypothesize about the neutrino mass spectrum in normal or inverted hierarchies (see Figure 1–5). However, since oscillations are sensitive only to the differences in the squares of the neutrino masses, it is currently difficult to determine the mass of an individual neutrino[29]. Still, we can provide certain mass constraints through various experiments.

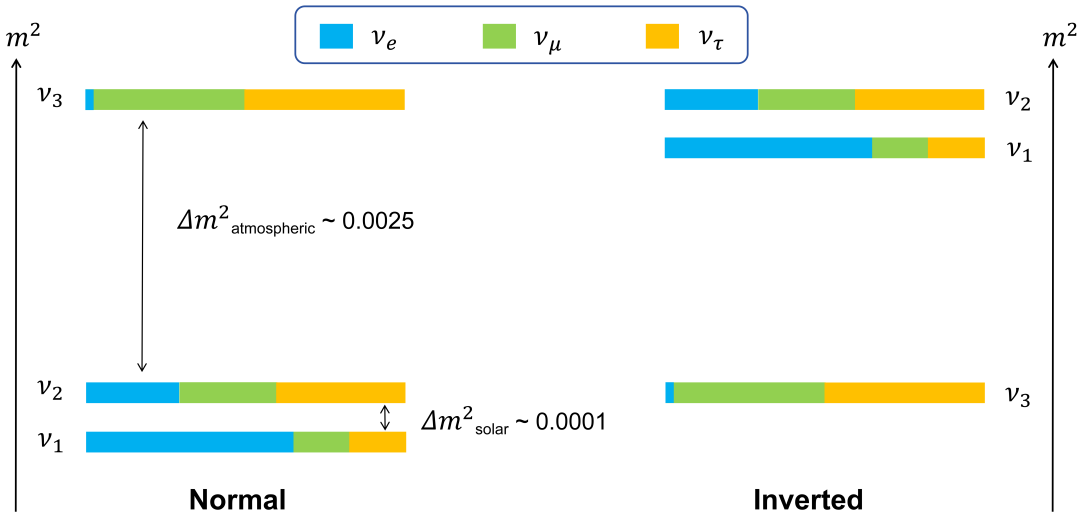

Figure 1–5 The pattern of neutrino masses for the normal and inverted hierarchies. Different color combinations reflect the mixing ratios of the three different mass eigenstates of neutrinos. The unit is $(eV/c^2)^2$.

It is important to emphasize that the neutrinos we commonly talk about (such as the electron neutrinos) do not have a definite mass. It is the mass eigenstates, ν_1, ν_2 and ν_3, that actually have definite mass. The flavor of a neutrino is just a characteristic that changes over time, not its essence. As we can see from Figure 1–5, when we try to express the mass

eigenstates in terms of flavor states, the majority of ν_1 is ν_e, ν_2 is essentially a mix of the three flavors with no significant difference, and ν_3 is mainly a half-and-half mix of ν_μ and ν_τ, with a tiny amount of ν_e. Of course, current experiments are still unable to tell us the exact values of these proportions.

1.3 Summary

In the first chapter, we briefly introduced the research history and some basic knowledge about dark matter and neutrinos, which are two critical guests in today's rare decay experiments. Currently, the international scientific community has successfully detected cross sections of WIMP dark matter particles down to below 10^{-47} cm^2 for masses around tens of GeV. Similarly, the cross sections for neutrinos at the GeV energy scale are also on the order of 10^{-38} cm^2. This extremely low probability of interaction is precisely why these phenomena are referred to as rare decays. Such low detection rates highlight the challenges in experimental physics in identifying and studying these elusive particles.

The invisible dark matter comprises about five times the universe's ordinary matter. Its existence is inferred from various astronomical observations, such as the rotational speeds of galaxies and cosmic microwave background radiation. Despite numerous theoretical candidates, like WIMPs, axions, and sterile neutrinos, dark matter still has too much for physicists to discover. Neutrinos are almost massless and interact weakly with ordinary matter. Their direct detection marked a milestone in particle physics, leading to the discovery of neutrino oscillation—a phenomenon where neutrinos change their flavors over distance. This discovery highlights the Standard Model's inadequacy in explaining all observed phenomena. All these unknown physics are challenging scientists to devise more innovative detection methods and never stop their exploration. All these investigations make it clear that while much has been discovered nowadays, the quest to unravel the universe's mysteries continues.

Chapter 2 Rare Decay Experiments

Searching for rare events is crucial for discovering new physics beyond the SM. These events are called rare events because the half-lives of these reactions are really long. Taking neutrinoless double beta decay ($0\nu\beta\beta$) as an example, its half-life is more than 15 orders of magnitude longer than the universe age[30]. Due to energy constraints, many extremely rare decays can only be observed at high-energy colliders. However, many underground experiments have shown considerable competitiveness for rare events related to DM and neutrinos. Excellent experimental environments hundreds to thousands of meters below the surface can shield against most cosmic ray background radiation, which is why these experiments prefer to be conducted underground or within mountains. This chapter will focus on introducing the design concepts and physical objectives of several currently competitive DM and neutrino-related experiments to provide readers with a more specific and in-depth understanding of rare decay experiments.

2.1 Dark Matter Experiments

In the quest to detect DM, a multitude of experiments worldwide have been started. As depicted in Figure 2–1, dark matter detection experiments can be categorized into three types based on the interaction methods they primarily rely on: direct detection, which seeks signals from interactions between DM and SM particles; indirect detection, which looks for signals from the annihilation products of dark matter itself into SM particles; and collider-based detection, where dark matter particles are produced through collisions of SM particles. The WIMP model is particularly appealing, leading many large-scale underground experiments (using liquid xenon or liquid argon) to target it. Additionally, numerous experiments are exploring lighter dark matter models, like the axion. Below, we will introduce several experiments tailored to different detection technologies.

2.1.1 The LUX-ZEPLIN (LZ) Experiment

The LZ experiment is located at the Sanford Underground Research Facility (SURF) in Lead, South Dakota, USA, which was previously the site of the LUX experiment. The

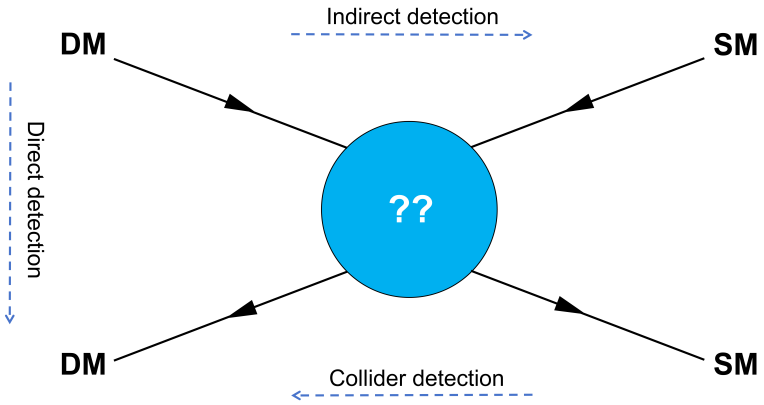

Figure 2–1 Detection methods for thermal dark matter by interacting with SM particles

LZ experiment is an upgraded version of the LUX and ZEPLIN-III experiments[31-32]. It is a direct detection search experiment to find cosmic WIMP dark matter particles. The Conceptual and Technical Design reports for the experiment were completed in 2015 and 2017[33-34], respectively. The experiment is expected to achieve a sensitivity of 1.5×10^{-48} cm^2 (90% C.L.)[35] for a WIMP with a mass of 40 GeV/c^2.

Figure 2–2 (a) displays a schematic cross-section of the LZ detector situated at the 4,850-foot level of SURF. The detector is encased in a water tank that shields it from external gammas and neutrons. The core of the experiment, the dual phase xenon time projection chamber (TPC), is housed within an inner cryostat vessel (ICV). Figure 2–2 (b) shows a schematic diagram of the assembled TPC. The effective height and diameter of the TPC are both 1.456 meters. Inside the TPC, 7 active tonnes of LXe are filled above the cathode, with an additional approximately 5.6 tonnes of fiducial mass[36].

Like other experiments that utilize a TPC for signal detection, the main detection principle of the LZ experiment involves detecting signals from secondary particles produced when WIMPs scatter off nuclei. These signals can be detected by Photomultiplier Tubes (PMT) arrays positioned above and below the interaction site. Specifically, the initial scintillation light signal and the recombination of electron-ion pairs both contribute to the formation of the S1 signal. Electrons that do not recombine are driven by an electric field to drift toward the gas-liquid interface, where they are extracted into the gaseous xenon by an extraction

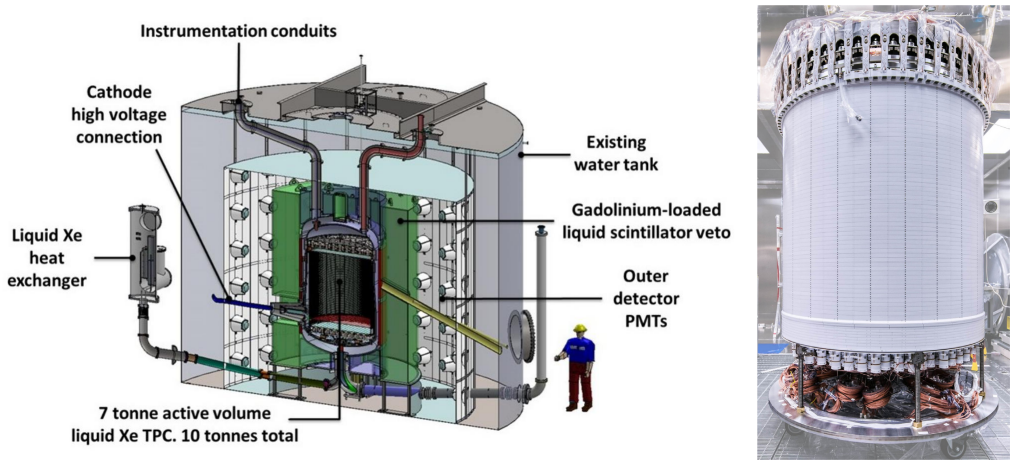

(a) The diagram of the LZ experiment. Taken from[33]

(b) The assembled TPC, photo by Matthew Kapust, Sanford Underground Research Facility. Taken from[36]

Figure 2–2 The major subsystems and TPC detector of the LZ experiment

field. Under the influence of a stronger electric field in the gas, these electrons collide with xenon atoms, causing electroluminescence and generating the S2 signal. The reconstruction algorithm uses the S2 signal to provide the horizontal location of the event, and the time interval between the fast-traveling S1 signal and the slower S2 signal offers information on the vertical position of the event. The nature of the interaction between a WIMP and a xenon atom, whether it is an electronic recoil ('ER') or a nuclear recoil ('NR'), can be inferred from the energy partitioning between the S1 and S2 signals.

2.1.2 The PandaX-4T Experiment

The PandaX (Particle AND Astrophysics experiment with Xenon) experiment is an international physics experiment led by Shanghai Jiao Tong University that focuses on the direct detection of dark matter and neutrinos. Established in 2009, the first phase, PandaX-I[37], equipped with a 120 kg liquid xenon target, began collecting data in 2014. The second phase, PandaX-II[38], featuring a 580 kg liquid xenon target, started data collection in 2016. The third generation of the experiment, PandaX-4T, which uses a 3.7 t liquid xenon target, began a trial run in November 2020 and is expected to accumulate data up to an exposure of 6 ton-years. The experiment is located at the China Jin-Ping Underground Laboratory (CJPL) in Sichuan, China, situated under approximately 2400 meters of rock. The laboratory houses two exper-

imental halls, CJPL-I and CJPL-II, which are shared by multiple experiments. In 2021, the results from the commissioning run provided a stringent limit on the cross-section of dark matter-nucleon spin-independent interactions at 3.8×10^{-47} cm^2 (90% C.L.)[39] for a WIMP with a mass of 40 GeV/c^2.

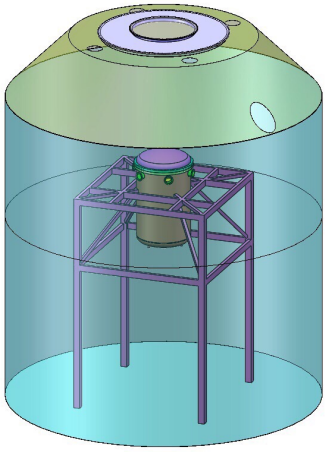

(a) The conceptual view of the ultrapure water shield for PandaX-4T experiment. Taken from[40]

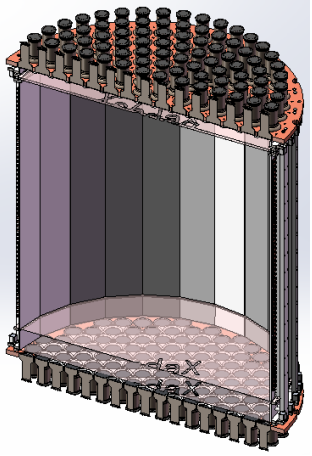

(b) Cross sectional view of the PandaX-4T TPC. Taken from[40]

Figure 2–3 The water tank and TPC of the PandaX-4T experiment

The PandaX-4T detector is housed within an ultrapure water tank, as shown in Figure 2–3(a), to shield it from external gamma rays and neutrons. The TPC is placed inside an inner vessel made of low-background stainless steel. Surrounding this, an outer vessel provides vacuum thermal insulation for the inner vessel. The design of the TPC is cylindrical, as illustrated in Figure 2–3(b), with a diameter of 1.2 meters and a height of 1.3 meters. Within the TPC, the gate and anode employ grid electrodes to provide high voltage and enhance transparency, while the cathode uses wire electrodes. The detection principle of this detector is similar to that used in the previously mentioned LZ experiment. The experiment will contain a total of approximately 6 t of liquid xenon, with about 4 t located within the sensitive volume of the TPC.

2.1.3 The DarkSide-20k Experiment

The DarkSide-20k experiment is a collaborative effort initiated by the Global Argon Dark Matter Collaboration (GADMC), which is mainly composed of four world-leading liquid

argon dark matter projects: ArDM, DarkSide-50, DEAP-3600 and MiniCLEAN. Located deep underground at the Laboratori Nazionali del Gran Sasso (LNGS), this experiment plans to operate a liquid argon time projection chamber (LAr TPC) with a total exposure of 200t yr. It aims to achieve a search sensitivity of 7.4×10^{-48} cm^2 for 1 TeV/c^2 WIMPs[41].

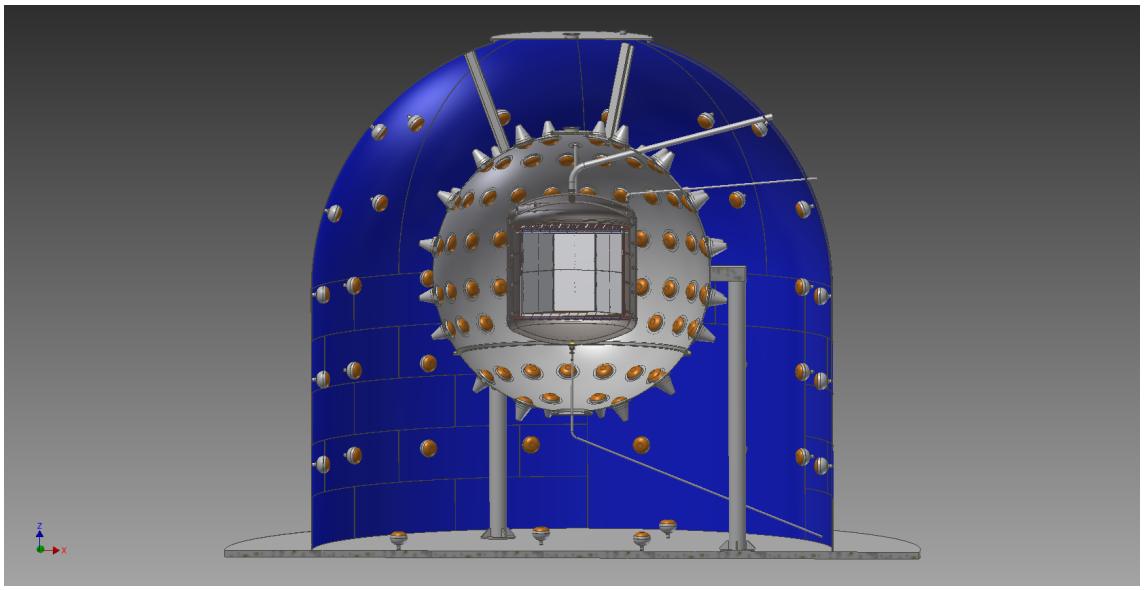

Figure 2–4 The conceptual drawing of the DarkSide-20k experiment. Taken from[41]

Figure 2–4 illustrates the cross-sectional view of the detector for the DarkSide-20k experiment[41]. The entire detector will be housed within a massive water tank in Hall C of the LNGS. A stainless steel spherical surface features a 6.6-meter diameter flange, ensuring an access path to the LAr TPC. Building on the success of DarkSide-50, the external structure of DarkSide-20k comprises a large cryostat chamber, designed to shield against cosmic radiation. Inside the cryostat lies the veto chamber, which serves to eliminate background signals from WIMP-nucleon collisions. At the core of the setup is the TPC, which is the principal detector of the DarkSide-20k experiment. The detection principle of the TPC is similar to that described in the previous chapter for the LZ experiment. However, unlike the TPC discussed earlier, the DarkSide-20k experiment does not use PMTs but instead employs Silicon Photomultiplier (SiPM) arrays to detect collision events. This update is expected to improve single photon resolution, increase photo-detection efficiency, and reduce background, given the intrinsic radiopurity of silicon.

2.2 Neutrino Experiments

Research on neutrinos is slightly more transparent than today's dark matter studies, but many crucial open questions are still awaiting exploration. For instance, the exact mass ordering of neutrinos, precise measurement of neutrino oscillation parameters, studies on sterile neutrinos, measurements of neutrinoless double-beta decay, and neutrino coherent scattering are all areas of active inquiry. Below, we will briefly introduce several planned or ongoing underground neutrino experiments.

2.2.1 The Jiangmen Underground Neutrino Observatory (JUNO)

The JUNO experiment was first proposed in 2008 and approved in 2013, and its Conceptual Design Report was published in 2015[42], followed by some further optimizations. The experiment is located in an underground laboratory beneath over 700 meters of mountain rock, approximately 53 kilometers from the Yangjiang and Taishan Nuclear Power Plants (NPP) in Guangdong, China. This location offers the best sensitivity for determining the mass ordering of neutrinos. The experiment aims to address various vital issues in neutrino and astroparticle physics with excellent energy resolution and a sizeable fiducial volume. Its primary goal is to determine the neutrino mass hierarchy with a 3–4 σ significance. The related physics objectives have been detailed in the JUNO Yellow Book[43].

The JUNO detector is filled with 20 kilotons of liquid scintillator (LS). As illustrated in Figure 2–5, the central detector (CD) is a liquid scintillator detector housed within a spherical acrylic vessel. It is expected to achieve an energy resolution of $3.02\%\sqrt{E(\mathrm{MeV})}$[44]. The CD is submerged in a 44-meter-tall water pool designed to shield against surrounding radioactive particles. This water pool is equipped with PMTs to detect Cherenkov light produced by cosmic muons. Above the water pool is a Top Tracker (TT), essentially a muon tracker, which is used to detect the directions of muons accurately.

The main signals in the JUNO experiment come from the antineutrinos emitted by nuclear reactors. The experiment detects electron antineutrinos through the inverse beta decay (IBD) interaction, as demonstrated in Equation 2–1 . The positrons produced rapidly deposit energy and ultimately annihilate to produce two 511 keV photons. This prompt energy includes the kinetic energy of the positron and the annihilation energy of the two 511 keV photons. Meanwhile, neutrons are captured by hydrogen or carbon atoms and release a 2.2

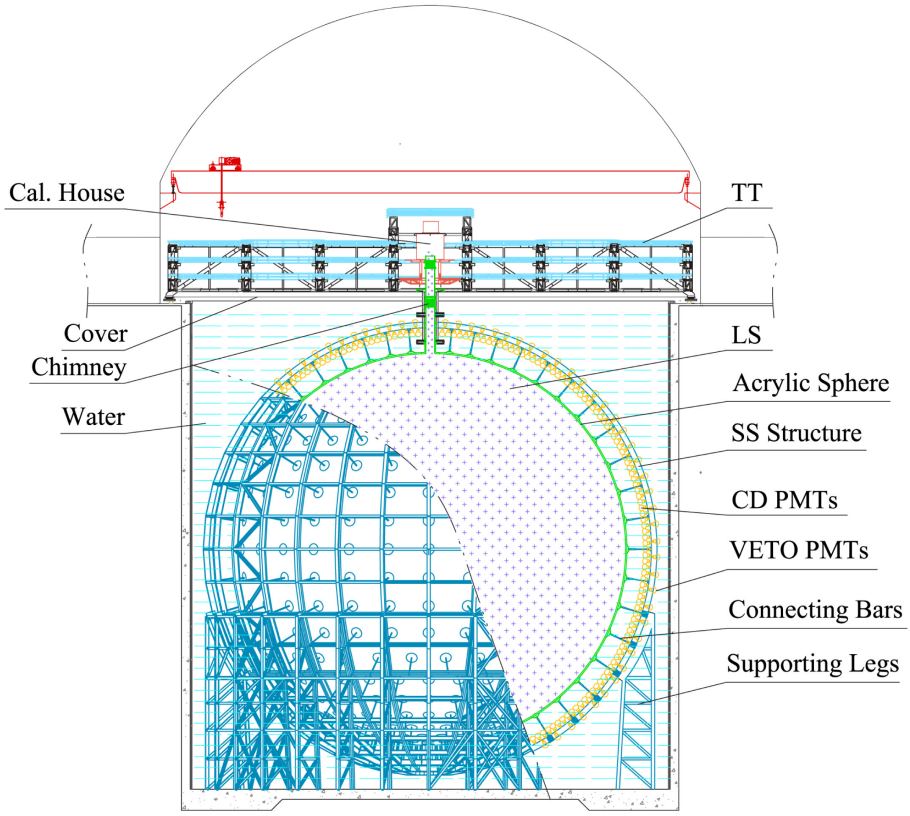

Figure 2–5 Schematic view of the JUNO detector. Taken from[44]

MeV photon about 200 μs later, providing a delayed signal. Additionally, JUNO can also measure neutrinos' properties by utilizing various neutrino sources such as solar neutrinos, reactor neutrinos, beam neutrinos, etc. These diverse sources enable comprehensive studies across different environments.

$$\bar{\nu}_e + p \longrightarrow e^+ + n \tag{2–1}$$

2.2.2 The Next Enriched Xenon Observatory (nEXO)

The nEXO experiment, proposed by the nEXO collaboration, was outlined in the Pre-Conceptual Design Report published in 2018[45]. Building on the foundation of the EXO-200 experiment, which successfully operated from 2010 to 2018 at the Waste Isolation Pilot Plant (WIPP) underground site in New Mexico, the nEXO aims to enhance the mass of liquid xenon (LXe) and upgrade the detector for a more sensitive search for neutrinoless double beta decay in ^{136}Xe. It is expected to achieve over a 100-fold increase in sensitivity compared to

EXO-200. The nEXO experiment plans to collect data over a decade to reach a sensitivity equivalent to 9.2×10^{27} years (90% C.L.).

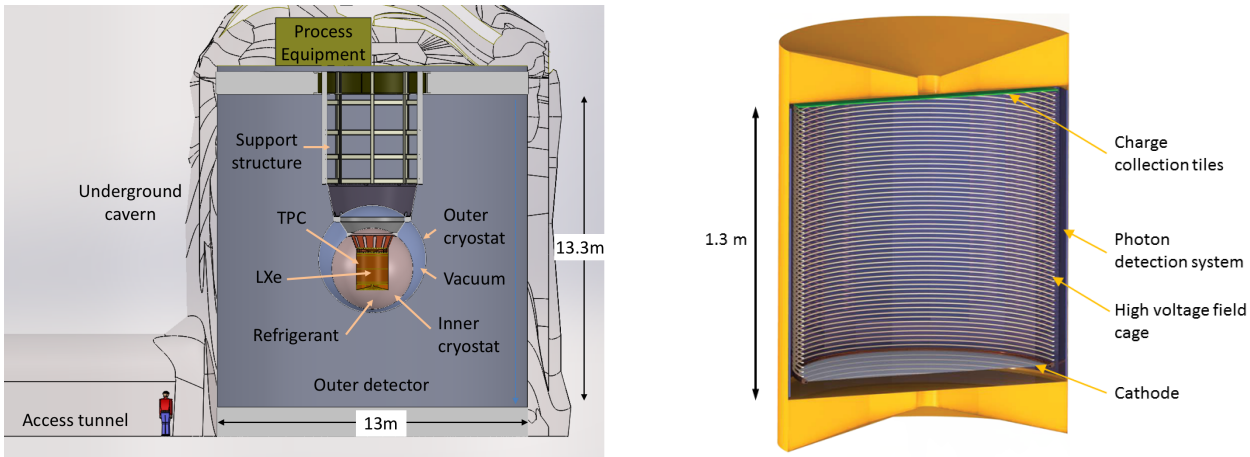

(a) Overview of the nEXO detector concept. Taken from[45]

(b) The cross section of the TPC of the nEXO experiment. Taken from[46]

Figure 2–6 Conceptual sketch of the nEXO experiment and TPC detector

Although the final location of the underground facility has yet to be confirmed, Figure 2–6 in the report presents a schematic assuming the detector will be placed in the underground Cryopit at the Sudbury Neutrino Observatory Laboratory (SNOLAB) in Sudbury, Ontario, Canada. The nEXO experiment's LXe TPC and cryogenic system are primarily based on the designs from the EXO-200 experiment. The TPC will be housed inside a massive water tank in a large double-walled cryostat filled with a fluorinated organic fluid (HFE-7000 by 3M). This setup provides shielding from external gamma rays and fast neutrons while ensuring the LXe temperature remains stable over long periods.

The nEXO experiment's TPC will contain 5 tons of 90%-enriched liquid xenon. Unlike previous detectors that featured two back-to-back TPCs with a common cathode, the nEXO TPC has a single cathode and anode, making the detector a homogeneous unit. This design reduces the internal radioactive background and utilizes γ-attenuation in LXe more effectively. The nEXO experiment employs VUV-sensitive SiPMs for light readout to collect xenon scintillation light. The SiPMs are positioned around the edge of the TPC, behind the field shaping rings. To achieve an energy resolution of 1% at the 2.5 MeV xenon Q-value, nEXO has optimized the use of plastics in direct contact with LXe, thus omitting the use of PTFE reflectors inside the TPC. However, some surfaces, such as the field shaping rings, are

made reflective.

2.3 Summary

This chapter highlighted several competitive experiments that will search for rare events in exploring physics beyond the SM. Due to their extremely long half-lives and sensitivity to background noise, these rare events require specialized underground laboratories and ultra-low radioactive detectors to search them accurately.

For DM research, two leading experiments included in the Generation 2 (G2) Dark Matter experiment program in the 2023 P5 report were examined: the LZ experiment and the DarkSide-20k experiment. Both of these experiments focus on direct detection but use different targets. The LZ experiment uses a dual-phase xenon TPC to detect cosmic WIMP dark matter particles and has started data-taking in 2021. The DarkSide-20k experiment employs a liquid argon TPC with SiPM arrays to improve detection efficiency at the LNGS in Italy. Data-taking of the DarkSide-20k experiment is scheduled to begin around 2025. Additionally, the China-based PandaX experiment has demonstrated significant competitiveness in the race for dark matter direct detection. The experiment is expected to be upgraded to a multi-ten-tonne scale liquid xenon experiment (PandaX-xT) to approach the "neutrino floor". All these experiments aim to significantly enhance the sensitivity to the cross-section of WIMPs.

This chapter also introduced two underground projects for neutrino experiments: the JUNO and nEXO experiments. JUNO, situated beneath over 700 meters of mountain rock in Guangdong, China, aims to address critical questions in neutrino physics, including determining the neutrino mass hierarchy. It uses a large liquid scintillator detector with excellent energy resolution. nEXO, with a considerable probability of being located at the SNOLAB, is designed to explore neutrinoless double-beta decay using a single-phase xenon TPC. It is worth mentioning that the JUNO experiment aims to begin the data-taking around 2024, which will be 4-5 years earlier than the DUNE experiment and give the result of neutrino mass hierarchy faster. After that, JUNO physicists plan to upgrade it to an experiment focusing on the NLDBD problem around 2030.

Together, these experiments represent the forefront of research into rare events, aiming to unravel the mysteries of dark matter, neutrinos, and other phenomena beyond the SM. Through sophisticated experimental setups, sensitive detectors, and rigorous shielding from

cosmic and background radiation, these projects continue to push the boundaries of our understanding of the universe.

Chapter 3 Radon Backgrounds in Underground Experiments

In experiments designed to detect rare events, the target events often have extremely low rates and can be overwhelmed by a large number of background noise. Consequently, controlling the experimental background's level and clearly understanding the residual background is crucial. In most deep underground experiments, including those mentioned previously, radon background is a significant challenge. Its ubiquitous and pervasive nature makes its complete elimination nearly impossible. Particle physicists can take two main approaches: first, selecting materials with lower levels of radioactivity for constructing detectors, and second, performing thorough and efficient cleaning of these materials before use to minimize their radioactive content. To date, various methods for radon removal or precise measurement of radon emanation rates have been developed and implemented. In this chapter, we will discuss the sources of the radioactive element radon in experiments, its impacts, and conclude with some typical experimental apparatus and methods currently used for measuring or removing radon.

3.1 Properties and Origins of Radon

Radon, with an atomic number of 86, is a colorless, odorless, noble gas at standard temperature and pressure (STP), making it undetectable by the human senses. All 39 isotopes of radon are radioactive, with mass numbers ranging from 193 to 231. The relatively stable isotopes, ^{222}Rn and ^{220}Rn, originate from the decay chains of ^{238}U and ^{232}Th, respectively (see Figure 3–1). Although radon has a short half-life, its continuous production through these long decay chains allows it to persist on Earth for extended periods. Radon's radioactive decay produces several other radioactive nuclei, known as "radon daughters", which are significant background sources in rare event detection experiments. Additionally, these particles can easily attach to dust and be inhaled, posing health risks to humans. Notably, ^{222}Rn has been classified as a carcinogen by the International Agency for Research on Cancer.

Due to the presence of radon-rich rocks and groundwater around underground laboratories, radon can diffuse into the air. Additionally, the materials used to construct detectors

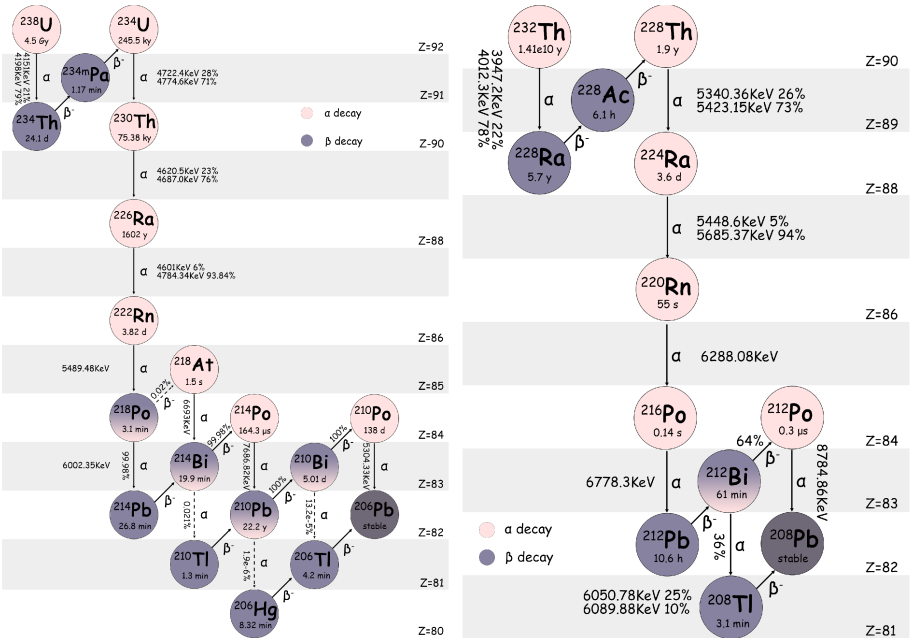

Figure 3–1 Decay chain of ^{238}U and ^{232}Th. Taken from[47]

typically contain radioactive elements such as ^{238}U, ^{232}Th, ^{137}Cs, and ^{60}Co. Of these, ^{238}U and ^{232}Th undergo decay processes that release radon gases ^{222}Rn and ^{220}Rn. Most radon in experiments comes from air leaks or radon emanation from materials used to construct detectors. As shown in the left subplot of Figure 3–1, ^{222}Rn originates from the decay of ^{238}U and has a half-life of 3.82 days. The ^{222}Rn eventually disperses into the sensitive volume of the detectors, contributing to the background signals. On the other hand, ^{220}Rn, which stems from the decay chain of ^{232}Th, has a much shorter half-life of 55 seconds. For a time, it was believed that ^{220}Rn's contribution to the experimental background could be negligible due to the minimal amount of gas released from materials and its short half-life. However, increasing experimental demands and subsequent simulations have shown that ^{220}Rn can contribute to the beta spectra background in experiments. More details on this will be discussed later.

3.2 The Impact of Radon Backgrounds in Rare Decay Experiments

3.2.1 ^{222}Rn Chain

From the decay chain shown in Figure 3–1, we observe that the decay of ^{222}Rn becomes a source of alpha particles. These high-energy alpha particles can deposit energy in the MeV

range, ionizing the target atoms in the detector and leading to high recombination yields. Furthermore, these alpha particles may also interact with nuclei in detector materials, such as fluorine in Teflon, in (α, n) reactions[48] to produce neutrons (see Equation 3–1). These neutrons, due to their scattering within the detector, are also common contributors to background events.

$$\alpha + {}^{19}F \longrightarrow n + {}^{22}Na \tag{3–1}$$

In addition to producing alpha particles, this decay chain also includes several beta-emitting radioisotopes. Among them, ^{210}Pb has a half-life of 22.2 years, which is long enough to ensure that it and subsequent daughter nuclei can be absorbed onto the cathode or be flushed out of the detector with the circulation system before decaying. Therefore, the impact of decay following ^{210}Pb can be disregarded. However, the potential for ^{210}Pb and its progeny leaching off surfaces requires further study[49]. Additionally, the impact of ^{214}Bi is not a significant concern. ^{214}Bi decays to ^{214}Po through beta decay, and ^{214}Po, with a half-life of only 164 μs, quickly emits a high-energy α. Thus, these events can be identified and excluded through β-α coincidence detection. Therefore, only the beta decay signals from ^{214}Pb need to be considered for their contribution. This is also why ^{214}Pb is the principal background in the energy range of dark matter.

3.2.2 ^{220}Rn Chain

The contributions of alpha particles and neutrons to the background in the decay chain of ^{220}Rn are similar to those in the ^{222}Rn decay chain. Taking the previously mentioned LZ experiment as an example, Figure 3–2 displays the alpha energy spectrum of its background, providing some insights into the proportional contributions of various isotopes. It's worth noting that the portions for ^{216}Po and ^{220}Rn are not shown. This is because ^{216}Po is not well-resolved in the displayed range, and the contribution from ^{220}Rn is minimal and overlaps with that of ^{218}Po, making it too difficult to identify.

The contributions to the remaining background from both decay chains are also quite similar. Due to ^{212}Bi having a short-lived daughter, ^{212}Po, with a half-life of only 300 ns, they can be identified through Bi-Po coincidence. ^{208}Tl undergoes beta decay, but it has no "naked" decay modes, meaning it can be identified through its observable accompanying

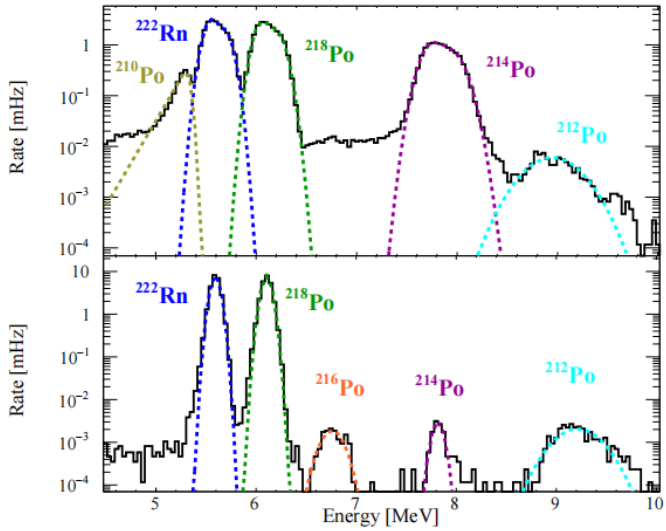

Figure 3–2 Comparison of alpha energy spectra in the LZ experiment: TPC events with basic cuts vs. SS events in fiducial volume. Taken from[49]

gamma rays, so it's not a significant concern. Therefore, only the contribution from ^{212}Pb needs to be considered. However, due to the shorter half-life of ^{220}Rn compared to ^{222}Rn, its concentration is significantly lower, leading us to expect that the activity of ^{212}Pb will be lower than that of ^{214}Pb.

3.3 Techniques for Radon Emanation Measurement and Removal

Controlling the radon background effectively requires various efforts. This section will introduce some major radon-related techniques used in current experiments with high background level requirements. Through these techniques, particle physicists aim to reduce radon background levels in their experiments and gain clearer insights into residual radon background situations.

3.3.1 Ultra-trace Radon Measurement System

Despite thorough cleaning procedures, radon gas can still emanate from the surface of materials. Therefore, we need detectors capable of accurately measuring the radon emanation rate from the materials used to construct experimental detectors. The most mainstream and effective method currently is the electrostatic collection of radon daughters, which can achieve measurement sensitivities several orders of magnitude better than commercial radon

detectors in low background experiments. Figure 3–3 shows a typical schematic of an electrostatic detector used in the SuperNEMO experiment[50], which is a neutrinoless double beta decay experiment. The interior of the detector chamber is made of electro-polished stainless steel[51]. Today, to achieve even lower background levels for the experimental detector itself, various polishing methods, including but not limited to mirror polishing, are being employed in the treatment of the electrostatic detector chamber. These treatments will help enhance the sensitivity of the detector to lower trace levels.

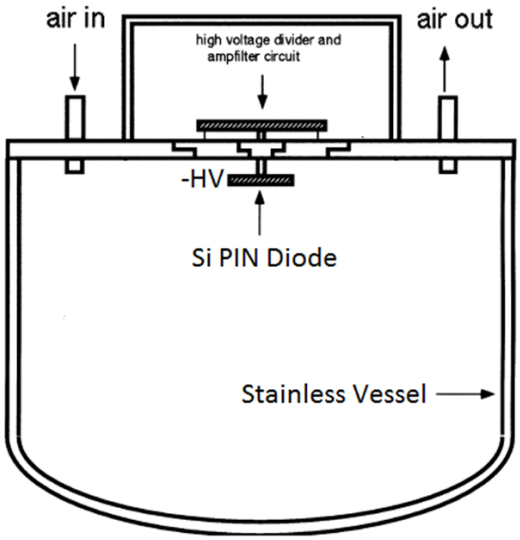

Figure 3–3 Schematic of the electrostatic detector for the SuperNEMO experiment. Taken from[51]

We will briefly explain the principle of this type of method using the classic detector structure shown in Figure 3–3. Typically, the metal detector chamber is grounded, and negative high voltage is applied to the detector through a bias circuit, specifically to the Si PIN Diode, thus establishing an electrostatic field between them. About 87.3% of radon progeny in the air carry is positively charged[52] because the recoil energy from alpha decay ionizes some of their outer electrons, leaving the nucleus with more positive than negative charges. Under the influence of the electric field, these positively charged ions are collected on the surface of the PIN Diode. Once they decay, particularly through alpha decay, they are likely to deposit energy in the detector, with the amount of energy being proportional to the generated charge. This data is ultimately recorded as waveforms, which will be used for subsequent energy spectrum analysis.

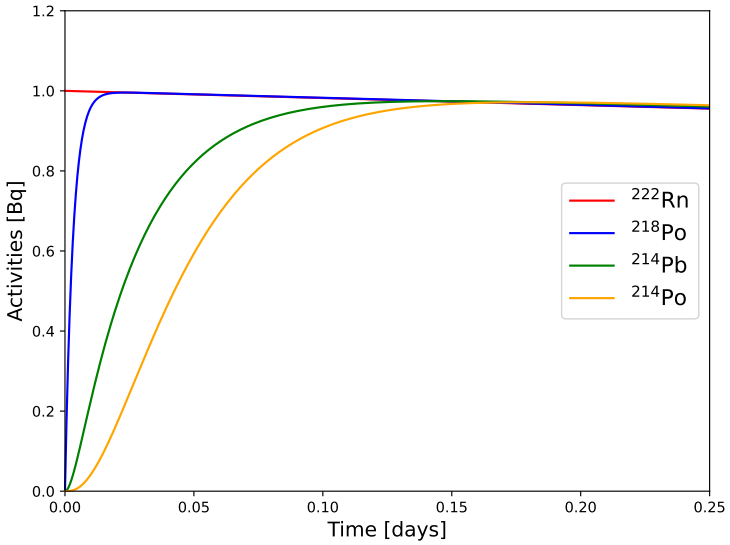

Figure 3–4 The scenario depicted in the figure assumes an initial introduction of 1 Bq of ^{222}Rn into the chamber. It shows that approximately after 0.17 days, the radioactive activities of various elements tend to converge.

In the experiment, we need to place the material to be tested inside the chamber, where radon from the material will continue to get released into the air over time. Figure 3–4 illustrates the variation in radioactive activity of different isotopes over time (in days) in this kind of process. After introducing 1 Bq of ^{222}Rn into the chamber, it only takes a few hours for the radioactive activities of all the nuclides to reach equilibrium with the radon gas. Therefore, by measuring the alpha decay rates of ^{218}Po and ^{214}Po at equilibrium, we can determine the radon number concentration and thus establish the level of the material's radon emanation rate.

3.3.2 Cold Trap Enrichment System

Many low background experiments require extremely stringent control of radon contamination, with some standards demanding less than 1 μBq/kg, a level often unachievable by the radon emanation chamber mentioned earlier alone. Therefore, for materials with exceptionally low radon backgrounds or volumes that exceed the capacity of the emanation chamber, we need to combine some new approaches to the radon detector, namely the cold trap enrichment system.

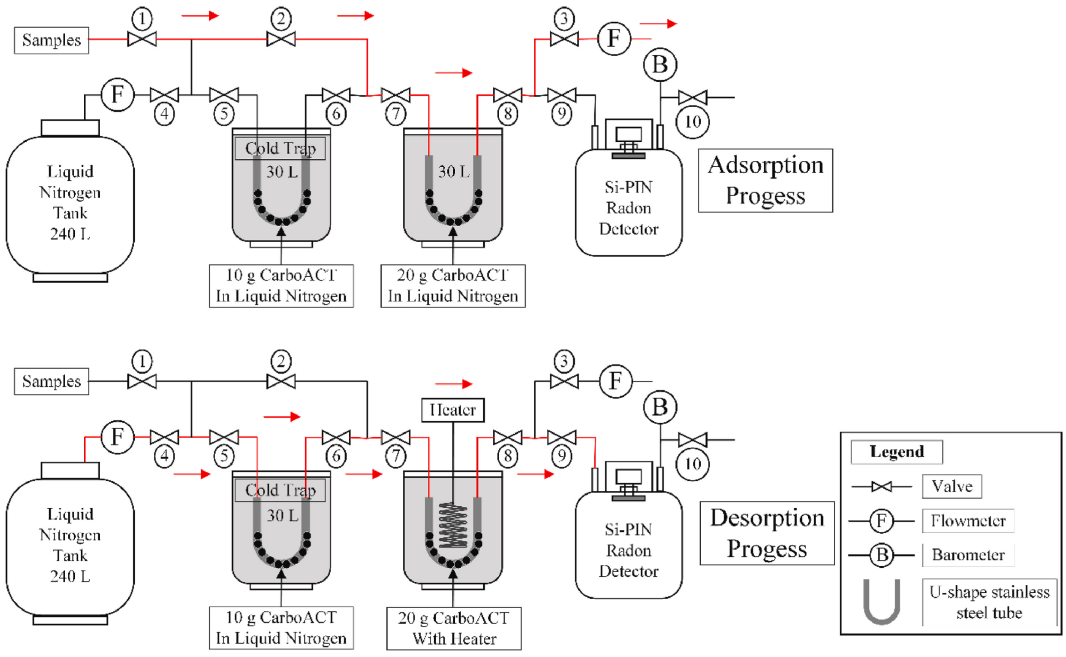

Figure 3–5 Schematic view of the cold trap enrichment system in the CDEX experiment. Taken from[53]

Figure 3–5 shows the radon measurement system used in the CDEX experiment, capable of detecting radon at the μBq/m^3 level[53] . This system combines a cold trap enrichment setup with electrostatic radon monitors, using flow controllers to manage the speed at which sample gas passes through the subsequent cold trap. During the radon absorption process, 20 g of activated charcoal is immersed in liquid nitrogen, which liquefies the radon gas using the cold temperature of the liquid nitrogen and steadily adsorbs radon from the sample gas. During the desorption process, the activated charcoal is heated to 200 °C to release the radon gas, which is then transferred from the cold trap to the subsequent radon detector for measurement by exploiting the pressure difference.

3.3.3 Activated Carbon Radon Removal System

Liquid xenon is considered one of the ideal target materials for many low background experiments due to its large mass number and the absence of long-lived radioactive isotopes among other advantages. Therefore, there is typically a need in these experiments to reduce the level of radon mixed with the xenon to extremely low levels. Since both Rn and Xe are noble gases, physical methods could be attempted to separate them. A common approach is

the use of an activated carbon trap. The differing van der Waals forces exerted by the activated carbon on each gas result in different propagation speeds through the carbon. Experiments have shown that the ratio of their mean propagation velocities in a trap at -85 °C is $v_{Rn}/v_{Xe} = (0.96 \pm 0.10) \times 10^{-3}$[54]. Effectively leveraging this characteristic can aid in reducing the overall radon concentration in the xenon carrier gas.

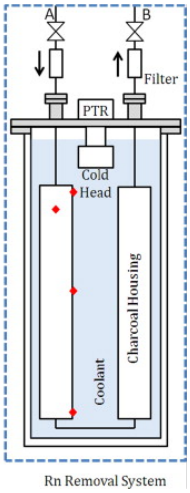

Figure 3–6 Schematic diagram of the activated carbon radon removal system in the XMASS experiment. Taken from[54]

Figure 3–6 shows a schematic of the activated carbon radon removal system used in the XMASS experiment. The trap is typically immersed in a coolant storage tank to maintain a low temperature (in this case, -85 °C). The system also allows the trap to be heated to 120 °C, enabling the activated carbon to release all previously adsorbed radon. This method facilitates the efficient removal of radon contamination from xenon gas. Furthermore, one can envision that if the trap's tubing is sufficiently long, a significant portion of the radon will decay before re-emerging from the column, thereby achieving more effective removal.

Figure 3–7 illustrates a radon reduction system used in the LZ experiment[55]. Due to the significant impact of water vapor and other impurities on the performance of the carbon trap, the system requires extremely pure rare gases. The SAES high temperature getter shown in the figure is employed to purify Xe and Ar gases during the experiment continuously.

Before each measurement, gas is passed through a series of connected pathways comprising a charcoal trap and two radon detectors to assess the radon background levels within the entire system channel. After the carrier gas passes through the ^{222}Rn source for three min-

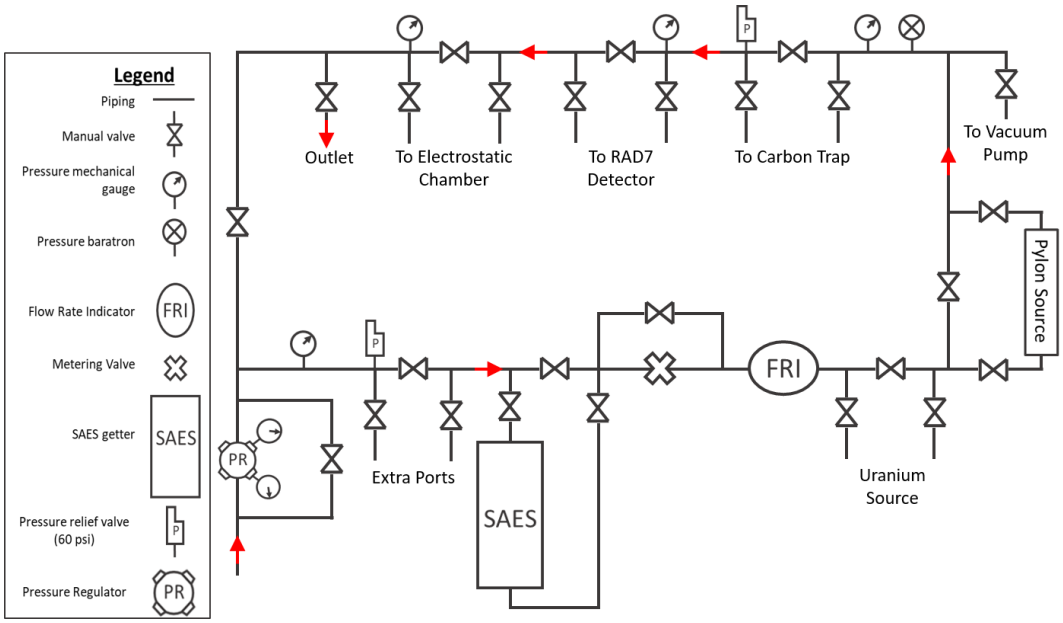

Figure 3–7 Schematic view of the radon reduction and evaluation system in the LZ experiment. Taken from[55]

utes, it enters the charcoal trap in a sharp, short pulse. During each measurement, the carrier gas continuously flows through the trap. The design of the gas system in this setup allows for the study of the adsorption effects of ^{222}Rn on charcoals under varying pressures. The detection principles of the subsequent electrostatic chamber are consistent with those mentioned earlier. Their experiments indicate that Saratech (Blücher GmbH.) is the commercial charcoal brand that can more efficiently remove radon. Additionally, treatment with high-purity nitric acid (HNO_3) etched can further reduce the intrinsic ^{238}U in Saratech, thereby further lowering its radon activity.

3.3.4 Radon Distillation Column

Another radon reduction strategy that can help us lower the radon levels in the target materialsis the radon distillation column. In this method, we primarily leverage the different saturated vapor pressures of radon and xenon at the same temperature. According to Raoult's law, radon tends to enrich in the liquid phase, while xenon is more prevalent in the gaseous phase. Therefore, we can separate xenon from radon by removing it from the top, while the radon remains trapped in the liquid xenon at the bottom until it decays. For the XENONnT experiment, as shown in Figure 3–8, this distillation column[56] will be a towering structure

at 3.8 meters tall.

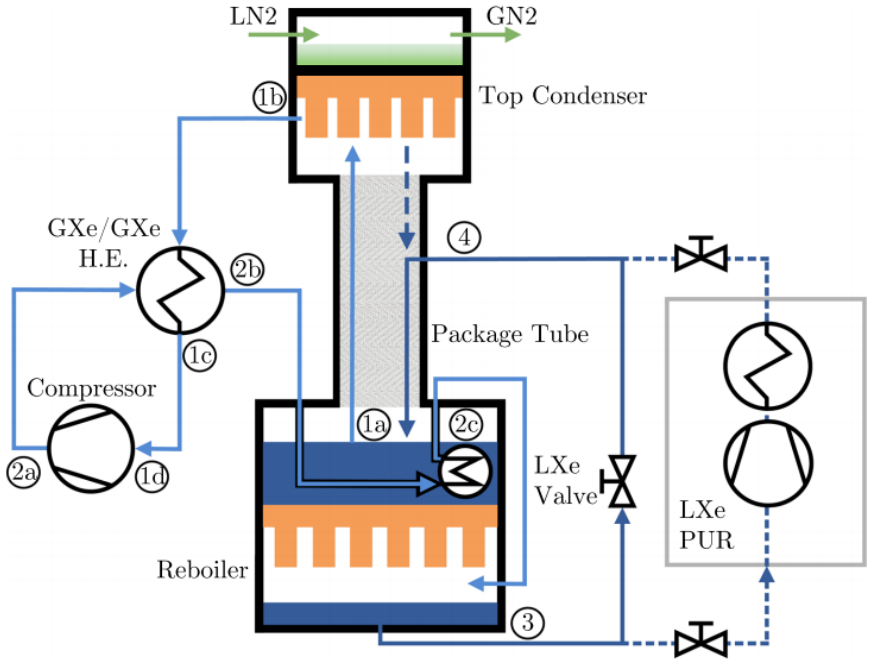

Figure 3–8 Schematic view of the radon distillation system for the XENONnT detector. Taken from[56]

Figure 3–8 shows the four main components of the radon distillation column: the package tube, the reboiler, the top condenser and the compressor. The package tube effectively manages liquid xenon flow and distribution. It ensures even distribution across its diameter and adjusts for thermal changes. The reboiler serves a dual function. Its top half is designed to trap ^{222}Rn until it decays, ensuring it does not re-enter the system. Secondly, it acts as a xenon-xenon heat exchanger. This setup facilitates the evaporation of xenon into the package tube and the re-liquefaction of purified xenon at the bottom. The top condenser creates a reflux with a ratio of 0.5, which enhances the separation efficiency. It provides 1 kW of cooling power using liquid nitrogen to maintain optimal temperatures and ensure the stability of the distillation process. The compressor features four radon-free, magnetically coupled piston pumps. These pumps re-liquefy gaseous xenon from the top condenser, ensuring continuous circulation and efficient xenon processing within the system.

This column can operate in two modes: LXe mode and GXe mode. In LXe mode, liquid xenon is directly extracted from the detector, purified, and then fed back into the detector.

GXe mode, on the other hand, involves extracting gaseous xenon to remove radon released both from within the detector and from external components such as tubing and cables. In this radon distillation column, combining both operating modes is expected to achieve a radon reduction by a factor of 4.7.

3.4 Summary

This chapter has discussed the significant challenge of radon backgrounds in underground experiments designed to detect rare events. The persistent and ubiquitous nature of radon, particularly the isotopes ^{222}Rn and ^{220}Rn, requires meticulous management to minimize their impact on experimental outcomes. Due to the radon's origin from the decay chains of ^{238}U and ^{232}Th, it is often present in the materials used to construct detectors and can infiltrate experiments via air leaks or material emanation.

Particle physicists employ two primary strategies to control radon levels: the selection of low-radioactivity materials for detector construction and the efficient and thorough cleaning of these materials. Additionally, we have reviewed several practical techniques currently employed to measure and remove radon, such as electrostatic collection of radon daughters for measurement and using activated carbon for radon removal. These methods have shown significant potential in reducing radon contamination levels in sensitive experimental setups.

In summary, while the complete elimination of radon is nearly impossible due to its natural ubiquity and the presence of radon-emitting materials within the experimental infrastructure, ongoing research and technological advancements provide effective strategies for managing radon levels. These efforts are vital for the success of experiments that depend on minimizing background noise to detect rare particle interactions.

Chapter 4 Symmetric Radon Diffusion Chamber Design

In recent years, the challenge of managing radon release and its diffusion has become increasingly significant for low background experiments. In practice, membrane materials have been employed to block radon and its progeny. In specific experiments like the JUNO experiment, a coating is applied to the detector's surface during construction to prevent radon penetration. Furthermore, these membrane materials are also utilized to shield the cleaned components of the detector during transport, safeguarding them from airborne radon infiltration. Nonetheless, the effectiveness of these materials is naturally limited by the permeation of radon gas. In evaluating this performance, various devices have been developed to measure the radon diffusion coefficient of different materials, ranging from membrane materials[57-58] to others such as concrete and air[59]. In this chapter, we will introduce a new detector with a symmetric radon detector cavity, leveraging the electrostatic collection technique of radon decay products discussed in the previous chapter. This innovative compact detector offers some fresh perspectives on determining the radon diffusion coefficients for various membrane materials.

4.1 Overview of the Experimental Setup

Figure 4–1 provides a detailed overview of the experimental setup for our system. The main components consist of two symmetrical cylindrical stainless steel chambers, each with a diameter of 0.165 m. The detailed geometric parameters of these chambers are shown in Figure 4–2 (a). The two sub-chambers are sealed in the middle by two O-rings, as depicted in Figure 4–2 (b). The test membrane can be seamlessly inserted into the central section. This O-ring design ensures the system is tightly sealed while preventing any damage to the membrane materials being tested, thereby avoiding gas leaks.

One of the sub-chambers is equipped with a 1/4 VCR connector in its center, which is used to connect a radiation source. In the experiment, we utilize a flow-through ^{226}Ra radioactive source, as shown in Figure 4–3. It contains a small amount of solid ^{226}Ra particles that continuously and stably produce ^{222}Rn. Filters and spherical valves are installed on both

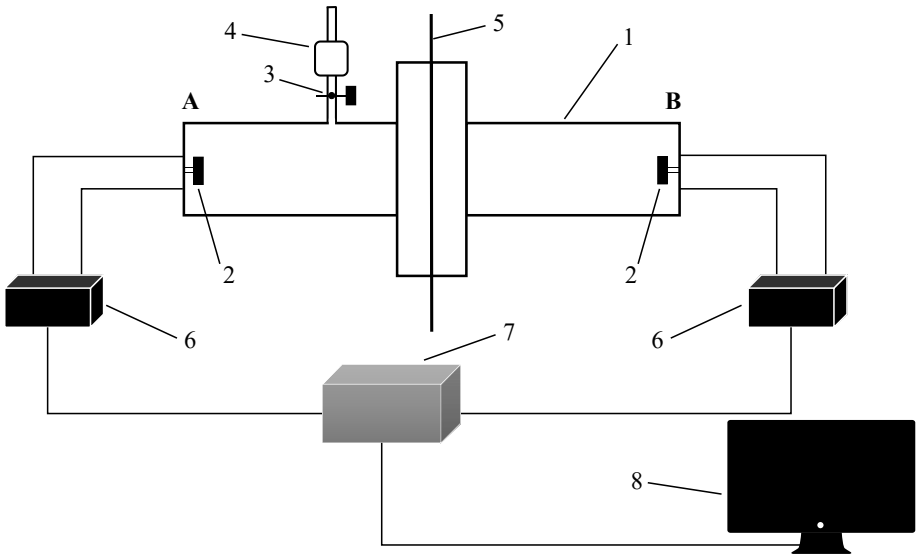

Figure 4–1 Diagram depicting the experimental arrangement: 1 - Stainless steel chamber; 2 - Silicon PIN diode; 3 - Ball valve; 4 - Radium source (^{226}Ra[60]); 5 - Membrane material for testing; 6 - Pre-signal amplifier box; 7 - Digital multi-channel analyzer (Digital MCA, DT5780[61]); 8 - Desktop computer.

sides of the tubing to control the on and off states of the radioactive source.

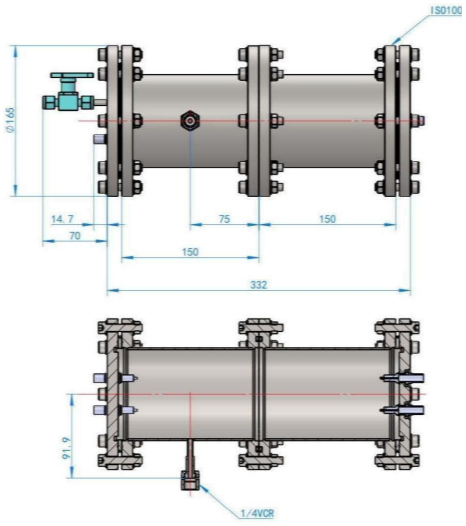

(a) Section parameter diagram of stainless steel cavity

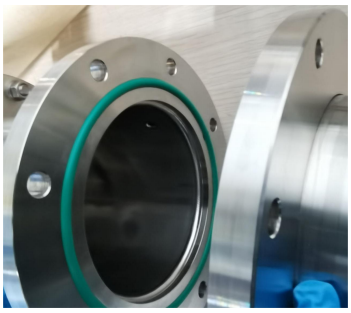

(b) Photo of the O-ring seal

Figure 4–2 Stainless steel cavity and O-ring seals display

Each sub-chamber is equipped with a pair of SHV-10 2-pin high vacuum coaxial feedthroughs

with embedded contacts, designed to install Si PIN Diodes. We use the S3204-09 model of commercial silicon PIN photodiodes[62] from Hamamatsu Corporation in Japan, which exhibit good energy resolution at room temperature (see Figure 4–4). We provide a working voltage of 70V to the Si PIN through a bias circuit, while applying a negative high voltage of -1600V to the silicon crystal.

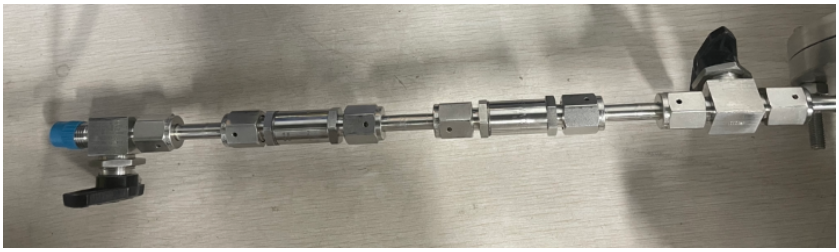

Figure 4–3 Photo of the gas type ^{226}Ra radioactive source

The silicon PIN diode produces an initial electrical signal that will be first amplified by a pre-signal amplifier. Figure 4–5 shows the circuit diagram for the bias circuit. Capacitors are included in the circuit to minimize the impact of noise from the power supply, and a capacitor at the signal output end is used to decouple AC signals from the DC high voltage. The circuit also features a ±12V power supply to provide the operating voltage for the preamplifier. At the same time, electrolytic capacitors are used to prevent damage to the preamplifier in case of reverse power connection. Two 50-ohm resistors in the circuit serve to match impedance at the signal end, and a series resistor circuit is used above to achieve voltage division.

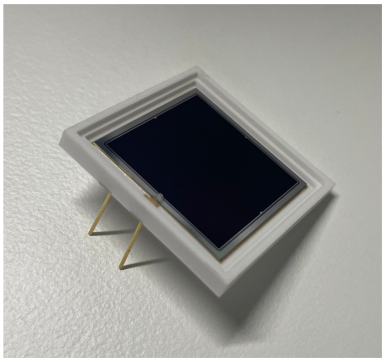

Figure 4–4 Photo of the silicon PIN photodiodes

The amplified signal is then transmitted to the multi-channel analyzer (MCA) and a personal computer (PC). For real-time data management, including readout and storage on the

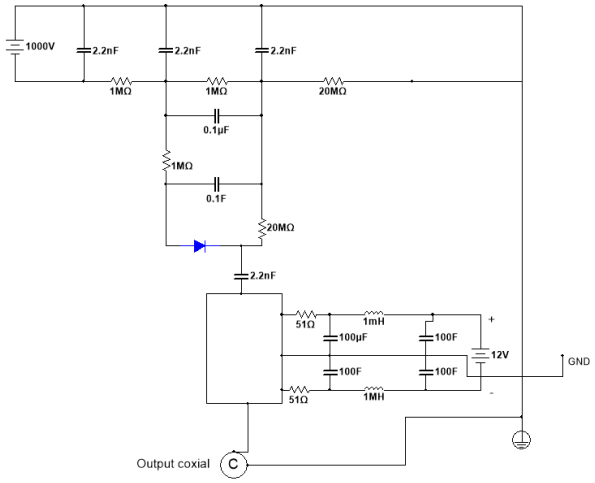

Figure 4–5 The circuit diagram of the bias circuit

PC, we utilize the *COMPASS* software. This program enables the observation of real-time energy spectra and the logging of spectral data over time. These spectra provide insights into the progression of the radon decay chain within the chamber.

To reduce measurement errors due to the cavity structure flanking the membrane, we engineered the cavity with a symmetrical design. The appropriateness of this design was confirmed by simulating the electrostatic field distribution given the system's current geometry and material characteristics. These simulations were conducted using *COMSOL* software, and the results are depicted in Figure 4–6. As expected, the diagram shows a clearly defined symmetrical electrostatic field. This symmetry is vital as it significantly reduces the effects of structural asymmetry on particle detection efficiency on both sides. Additionally, the negative high voltage configuration is designed to ensure effective attraction of the positron body towards the semiconductor within the electric field.

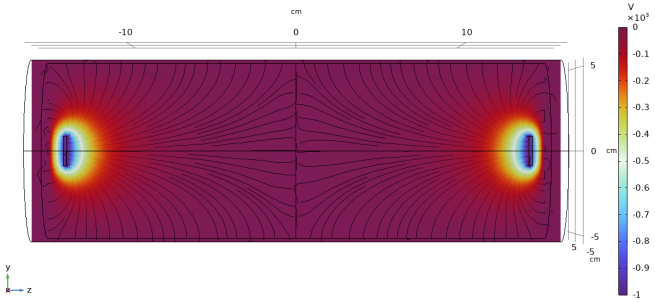

Figure 4–6 Simulation result of the electrostatic field

4.2 Radon Diffusion Model

The physical process of radon diffusion in our system is typically characterized by Fick's Law and the diffusion equation:

$$J = -D\nabla C \tag{4–1}$$

$$D\nabla^2 C - \lambda C = \frac{\partial C}{\partial t} \tag{4–2}$$

where J is the rate of radon flux per unit area, D is the radon diffusion coefficient, C is the radon number concentration in the chamber, and λ is the radon decay constant ($2.1\times10^{-6}s^{-1}$).

When investigating radon solubility in various materials, we observe a proportional relationship between radon concentrations inside and outside the membrane surface, as described by Equation 4–3. This finding aligns with prior research[63].

$$C_i' = SC_i \tag{4–3}$$

In this equation, C_i represents the radon number concentration outside the membrane, while C_i' denotes the concentration inside. The solubility of radon in the membrane compared to the gas phase is represented by S. At equilibrium time t, $C_i(t)$ can be measured using radon detectors positioned on both sides of the membrane. The subsequent sections will outline the method for obtaining these parameters by analyzing the radioactivity of radon daughters on each side of the membrane through our system.

We don't need to consider solubility S when calculating the average diffusion coefficient. By focusing on the external concentration C_B (where B indicates the side opposite the radium source), Equations 4–1 and 4–2 allow us to derive:

$$\frac{\partial C_B}{\partial t} = -\frac{D_a A}{V_B}\cdot\frac{C_B - C_A}{d} - \lambda C_B \tag{4–4}$$

where D_a is the average diffusion coefficient, A is the membrane surface area, d is the membrane's thickness, and V_B is the chamber volume on the B side. When equilibrium is reached, the number concentration on the left side of the equation remains constant, making it zero. Thus, Equation 4–4 in equilibrium state can be rewritten as:

$$D_a = \frac{dV_B\lambda}{A} \cdot \frac{\eta}{1-\eta} \tag{4–5}$$

where η is the ratio of radon number concentrations across the membrane:

$$\eta = \frac{C_B}{C_A} \tag{4–6}$$

Therefore, once the concentration ratio across the membrane is known, the average diffusion coefficient D_a can be easily calculated. This coefficient reflects the macroscopic influence of the membrane material on radon diffusion.

To explore the relationship between the precise diffusion coefficient and solubility more thoroughly, we can derive an expression similar to Equation 4–4 by assuming a one-dimensional space for simplicity:

$$\frac{\partial C_B}{\partial t} = -\frac{DA}{V_B}\frac{\partial C'_B}{\partial x} - \lambda C_B \tag{4–7}$$

When the system reaches equilibrium, the left side of Equation 4–7 equals zero. By following the approach described in the article[64], we can obtain the same transcendental equation:

$$\alpha \cdot \beta = \frac{S \cdot A}{V_B}\left[\frac{1-\beta\cdot\cosh(\alpha\cdot d)}{\sinh(\alpha\cdot d)}\right] \tag{4–8}$$

where we follow the established convention:

$$\alpha = \sqrt{\frac{\lambda}{D}} \tag{4–9}$$

$$\beta = \frac{C_B}{C_A} \tag{4–10}$$

In our experiment, we'll evaluate the solubility parameter, denoted as S, across a range of 1 to 20. The ratio of radon concentrations on either side of the membrane can be determined experimentally. Using this ratio and the specified S value, the radon diffusion coefficient D in Equation 4–8 can be calculated, resulting in a diffusion coefficient expressed as a function of solubility.

4.3 Analysis of Detector Performance and Spectral Observations

4.3.1 Characteristic Energy Peaks of Radon Decay Products

In the decay chain of ^{222}Rn, our detector can distinctly identify several monoenergetic α peaks, as depicted in the last chapter (see Figure 3–1). As shown in Figure 4–7, two prominent peaks are visible from left to right, corresponding to the peaks of ^{218}Po (6002.4 keV) and ^{214}Po (7686.8 keV). In fact, when the activity of the radioactive source is low and the measurement time is long enough, we can observe another relatively small ^{210}Po energy peak (5304.3 keV), as shown in Figure 4–8. However, with many events and extended measurement periods, this peak gets overwhelmed and becomes invisible.

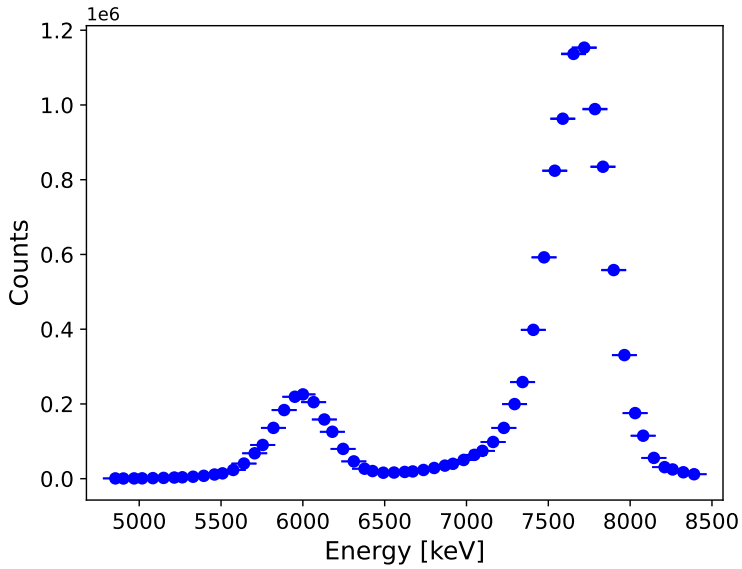

Figure 4–7 The two α characteristic peaks seen by our system, from left to right, correspond to ^{218}Po (6002.4 keV) and ^{214}Po (7686.8 keV). The data collection duration for this measurement was approximately 130 h.

The advantageous position of ^{214}Po further down the decay chain, compared to ^{218}Po, positively influences its collection efficiency. This occurs because both ^{214}Pb and ^{214}Bi, situated between them on the decay chain, can also be drawn to the Si PIN surface by the electric field and decay there. The subsequent ^{214}Po signals can still be detected by the detector. As indicated in Figure 4–7, the characteristic peak of ^{214}Po demonstrates a higher event count over the same collection time. Besides, distinguishing between events from ^{218}Po becomes challenging due to the substantial overlap between the energy peaks of ^{210}Po and ^{218}Po. Addi-

tionally, around 36% of ^{212}Bi decays via alpha decay, with an energy of about 6 MeV, which can also overlap with the ^{218}Po energy spectrum. Given these challenges, our subsequent analyses prioritize selecting the energy peak of ^{214}Po for nuclear radioactivity measurement to ensure improved precision in our results.

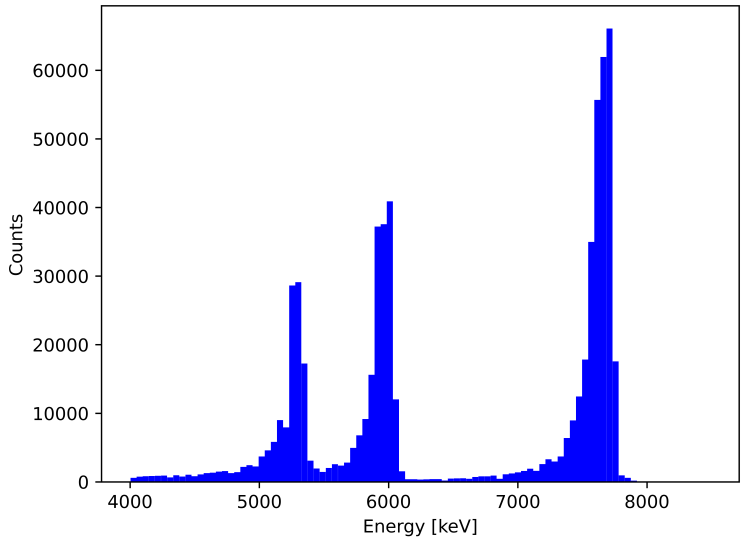

Figure 4–8 The alpha energy spectrum obtained at the background-level radiation. The peak on the far left corresponds to the ^{210}Po energy peak (5304.3 keV)

4.3.2 Calibration of the Detector

For the Radon Diffusion Chamber system, we aren't particularly concerned about the absolute efficiency of the two radon detectors. Instead, we focus on the ratio between their detection efficiencies, as our goal is to calculate the ratio of radon number concentration between the two sides.

To calibrate the system's efficiency, we connect the radon source, diffusion chamber, and RAD7 (a commercial radon detector[65]) in sequence. Throughout the process, we maintain a nitrogen flow rate of 1 SLPM to facilitate gas flow across the calibration setup, controlled via a Mass Flow Controller (MFC). After turning on the ^{226}Ra source, we wait until the radon concentration within the system reaches equilibrium before measuring. The calibration primarily focuses on detecting ^{214}Po efficiency, with results shown in Table 4–1.

There are two potential explanations for the 3.3% difference in efficiency between the two sides.

Table 4–1 Calibration for detection efficiency

Detection Position	^{214}Po (Bq/m^3)	Calibration Efficiency
RAD7	182.0±4.0	-
Detector Side A	55.9±0.6	30.7±0.8%
Detector Side B	49.9±0.6	27.4±0.7%

First, although the system was designed to be symmetric, uncontrollable factors such as variations in hand movements during pre-signal amplifier soldering and the angles at which silicon pins are placed can cause changes in detector efficiency. However, since the angle of the two silicon PIN diodes is consistent across all tests and each diode is linked to a specific pre-signal amplifier, any efficiency fluctuations arising from these factors are systematic and should not compromise the accuracy of our experiments.

Second, while continuous nitrogen flushing is employed to improve gas flow, the system's geometry can cause gas short-circuiting. In other words, the nitrogen inlet and outlet create a more direct gas path within the chamber, allowing nitrogen to exit quickly through this route instead of circulating throughout the chamber. This can result in uneven radon concentrations, with lower levels at the detector's farther regions. Future experiments aimed at optimizing the chamber design could mitigate this issue.

4.3.3 Background Levels

To assess the background level in the diffusion chamber, we operate the system with the ^{226}Ra source turned off. The signal rate of ^{214}Po on both sides of the membrane remains around 0.4 Bq/m^3. Each use of radioactive sources introduces variations in background counts for subsequent experiments, leading to inconsistencies. However, we have observed through comparative trials that the overall magnitude of background events remains consistent across experiments. Compared to the data in the previous subsection, the background level of the detector here is almost negligible compared to the radon concentration when the radiation source is open, which has little impact. Moreover, since the background levels during each experimental measurement vary, we have directly ignored the influence of the background in subsequent calculations without further processing.

4.4 Experimental Results

Based on the experimental setup and methods detailed in previous sections, we evaluated various membrane materials that are presently used in the PandaX and the JUNO experiments. The results of these measurements are presented in Figure 4–9.

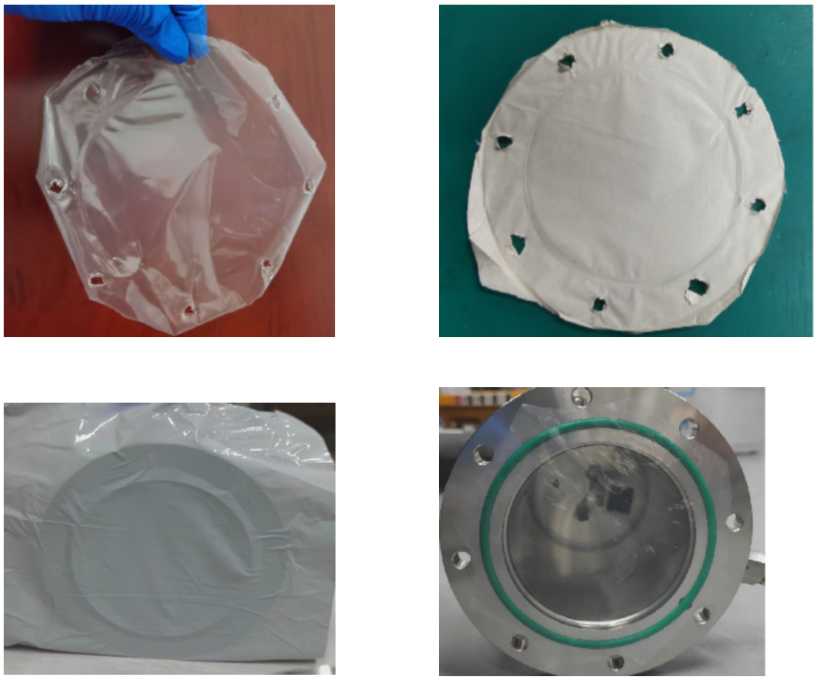

Figure 4–9 This figure shows the four membrane materials that we tested. The image in the top left corner features a nylon membrane, and the one in the top right corner shows a GOO.N paper membrane. The bottom left image displays a light-blocking film, and the bottom right image shows a polyethylene membrane.

After a specific period, the number concentration of ^{214}Po stabilizes on both sides of the membrane within the chamber (see Figure 4–10), signifying equilibrium in radon diffusion. As we have expected, the concentration levels on either side vary due to the presence of the membrane, where the radioactive activity of ^{214}Po in the receiver chamber is clearly lower than in the source chamber. By following the principles outlined in the last chapter, we can determine the relative concentration ratio of radon on each side by measuring ^{214}Po concentrations. This ratio is critical for evaluating the membrane's ability to inhibit radon diffusion.

Tables 4–2 and 4–3 present the parameters of four measured membrane materials in our experiments. All measurements were taken at room temperature (25°C). The parameter d rep-

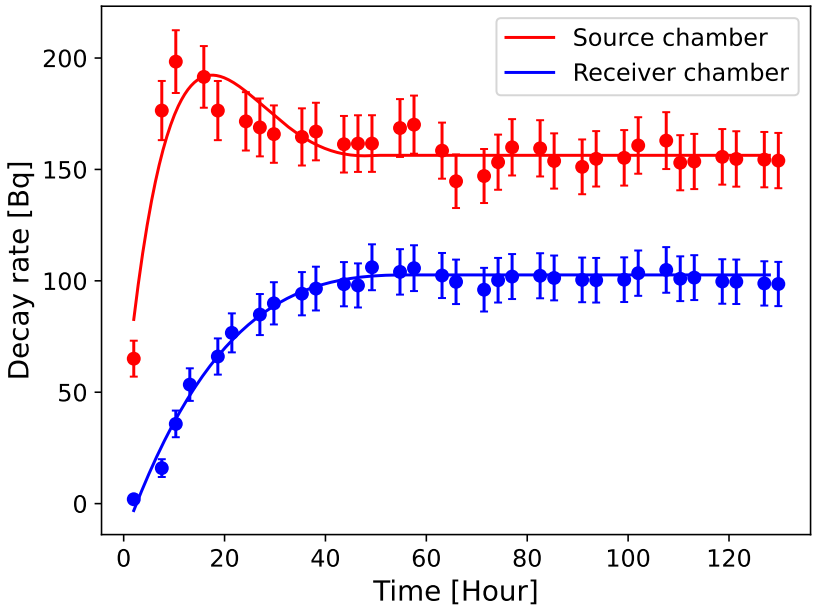

Figure 4–10 The image displays the progression over time of the radioactive activity of ^{214}Po on both sides of the membrane material while measuring the Paper (GOO.N) material. It can be observed that approximately 56 hours after activating the radiation source, the decay rate on both sides begins to stabilize.

resents the average membrane thickness, and η_R represents the relative radon ratio between the two sides, adjusted for detection efficiency. If C_i denotes the radon number concentration on side i and E_i represents the calibration efficiency for that side, the relative ratio η_R can be calculated using:

$$\eta_R = \frac{C_A/E_A}{C_B/E_B}$$

Table 4–2 List of parameters of measured materials (25 °C) - Part 1

	Nylon	Paper (GOO.N)
Translucent	Yes	No
d (mm)	0.083±0.002	0.053±0.002
Feature	Without glue	Single-sided water-soluble adhesive
η_R	0.1±0.01%	72.4±2.60%
D_a (cm^2/s)	(2.28±0.29)×10^{-10}	(4.40±0.50)×10^{-7}

The results distinctly reveal a wide range of diffusion coefficients across various materials. For instance, nylon exhibits a very low radon diffusion coefficient, effectively preventing

Table 4–3 List of parameters of measured materials (25 °C) - Part 2

	Light blocking film	Polyethylene
Translucent	No	Yes
d (mm)	0.077±0.002	0.089±0.002
Feature	Without glue	Single-sided minimal adhesive
η_R	92.1±3.40%	44.1±1.60%
D_a (cm^2/s)	(2.80±1.20)×10^{-6}	(2.21±0.11)×10^{-7}

radon diffusion. However, the light blocking film is much worse regarding the blocking function.

To identify the relationship between the radon diffusion coefficient and solubility, as explained in the previous section, we varied the solubility value S from 1 to 20 and calculated the corresponding diffusion coefficient D using Equation 4–8. Despite the fact that we didn't determine the exact S values due to experimental constraints, Figure 4–11 clearly shows the negative correlation between solubility and radon diffusion coefficient.

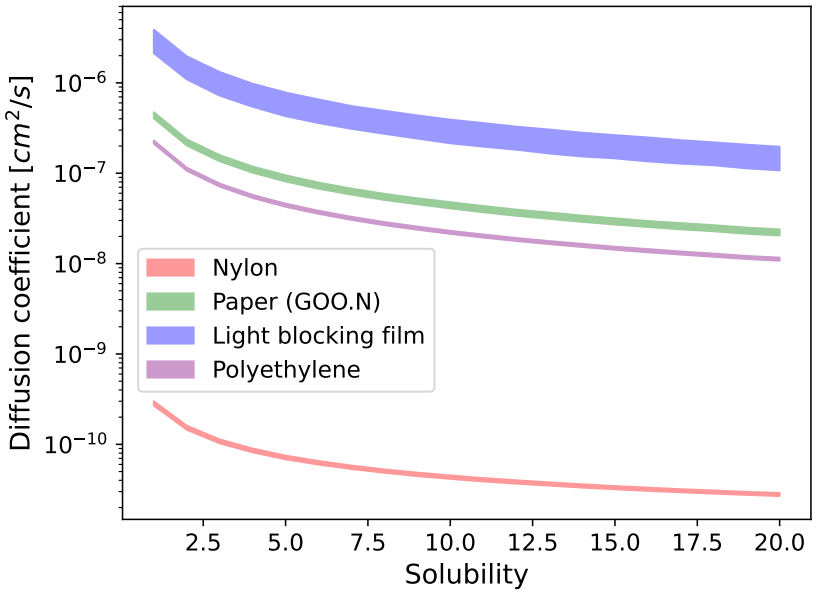

Figure 4–11 The figure presents the measurement results of the relative relationship between the radon diffusion coefficient and solubility. The curve band illustrates the results derived by varying S from 1 to 20 and applying Equation 4–7

The average diffusion coefficients for various materials align closely with those calculated when $S = 1$, consistent with physical expectations. Figure 4–12 contrasts the experi-

mental average diffusion coefficients with the theoretical coefficients for $S = 1$. The resemblance between these two sets of values across all materials verifies our hypothesis, offering a comprehensive comparison of the average diffusion coefficients among different materials. Hence, by using the average radon diffusion coefficient calculated from Equation 4–5, based solely on the difference in radon number concentration across the membrane, we can estimate the magnitude of a material's radon diffusion coefficient.

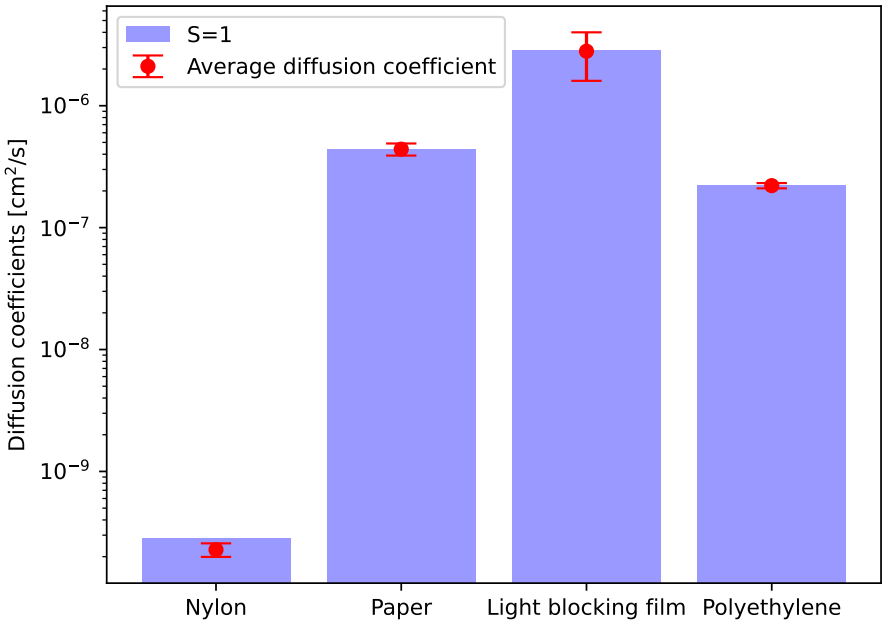

Figure 4–12 The red dots depict the average diffusion coefficient and error across different materials. Meanwhile, the height of the blue shading indicates the radon diffusion coefficient for each material, assuming $S = 1$.

4.5 Summary

In this chapter, we've introduced a symmetrical radon diffusion chamber design that improves upon the traditional electrostatic collection method, providing good capability for measuring the radon diffusion coefficient of radon across membrane materials.

We tested four different membrane materials, all of which are commonly used in low background experiments. Nylon's low radon diffusion coefficient shows promise for experiments requiring strict control over radon infiltration. Our results also underscore the influence of solubility on radon diffusion, and these findings on the impact of solubility may have

broader implications. Experiments involving rare decays and membrane materials must account for the material's intrinsic properties and environmental factors affecting solubility, such as temperature and humidity. Understanding the relationship between the diffusion coefficient and solubility for different materials is essential for assessing their effectiveness in preventing radon diffusion.

Chapter 5 Future Strategies for Radon Control and Measurements

In the previous chapters, we've discussed some experimental techniques and methods related to radon background. These approaches have been used in low background experiments for a long time and have generally been quite effective. In this chapter, I propose several ideas that could further control radon background in future experiments or use existing techniques to achieve new measurement objectives. Some of these ideas may already be under exploration, some might seem like a distant fantasy, and others face temporary technical challenges. Here, I offer my personal and tentative suggestions for reference.

5.1 Measurement of Radon Solubility Constants in Membranes

In the experiment from the previous chapter, specifically in the part about solubility, we only conducted a scan ranging from 1 to 20 without obtaining precise values. In fact, by making some adjustments to the experimental procedure and initial conditions, we could potentially use this radon diffusion chamber system to measure the radon solubility constant of membrane materials. A study[63] around 1991 discussed this topic. With today's detection technology advancements, we're poised to achieve even better measurement results.

To determine the solubility constants, we first need to ensure that the radiation source is turned off. Then, open the chamber and flush it with a nitrogen stream to clean it thoroughly. Place the membrane material to be tested inside, reassemble the chamber, and measure the radon background levels on both sides of the membrane. This experiment requires one sub-chamber to quickly increase from zero to a stable high radon number concentration. Therefore, we will need to supply a steady nitrogen flow throughout the experiment continuously.

We should connect the exhaust line of the sub-chamber closest to the radiation source to a gas delivery tube. The radiation source side is linked to the chamber on one side, and the other is connected to the nitrogen source through a gas flow meter. Naturally, this requires us to redesign the chamber's pipeline layout and the arrangement of the inlet and outlet gas channels to ensure that the nitrogen flow creates a consistent and stable radon concentration

environment in the sub-chamber connected to the radiation source. The new design will also compensate for the systematic errors that arise during calibration due to uneven radon concentration distribution. Once the entire system is ready for continuous data collection, we can turn on the radiation source and measure the radon concentration changes from the time the source is turned on until radon diffusion within the system reaches equilibrium. Subsequent calculations should refer to the methods described in the reference paper[63]. It's important to note that, due to technical limitations, the calculations in the paper only account for the total number of alpha decays. However, today's detectors can measure alpha energy to distinguish between different types of alpha decays. As a result, we should focus on monitoring changes in the concentration of specific decay products (say ^{214}Po) to achieve more accurate measurements of the solubility constants.

5.2 Methods for Controlling the Background Level of Radon Measurement System

To enhance the sensitivity of the previously mentioned radon measurement system, it's crucial not only to increase the detector's detection efficiency but also to reduce the radon background level within the detector's chamber. If the detector emits too much radon itself, the signals from materials with very low radon emanation rates could be drowned out by the detector's background radiation, making measurement impossible. Thus, reducing the detector's inherent background enables it to accurately measure materials with extremely low radon emissions. Typically, the radon background in detectors originates from radon emitted from the inner surface of the chamber, which is a result of the decay of uranium and thorium present in the construction materials. Therefore, besides prioritizing low-uranium and low-thorium materials during detector construction, new methods are needed to further reduce the background in the radon measurement system.

As mentioned in previous sections, surface treatments like electrochemical and mirror polishing can be applied to the inner surface of the detector chamber to reduce surface roughness. Generally, smoother surfaces translate to lower radon emanation rates, thereby improving detector sensitivity.

Additionally, the radon diffusion process from the detector material can be artificially

blocked. Using the double-chamber detector introduced earlier, we can identify membranes with excellent radon diffusion-blocking properties and low inherent radon emissions. These membranes can be tightly adhered to the inner surface of the detector chamber, effectively creating a protective layer that prevents radon diffusion. Mylar films, for example, are known for their low radon background and effective diffusion barrier properties. Such membranes can help further reduce the radon background of the radon measurement system.

Moreover, altering the structural design of the detector chamber might also help reduce the radon background. Typically, the volume of a chamber remains constant regardless of its shape. Whether measuring a small film or a larger PMT, the chamber volume is always the same. This insight suggests that the chamber volume could be manually reduced for smaller samples to optimize detection efficiency and background levels.

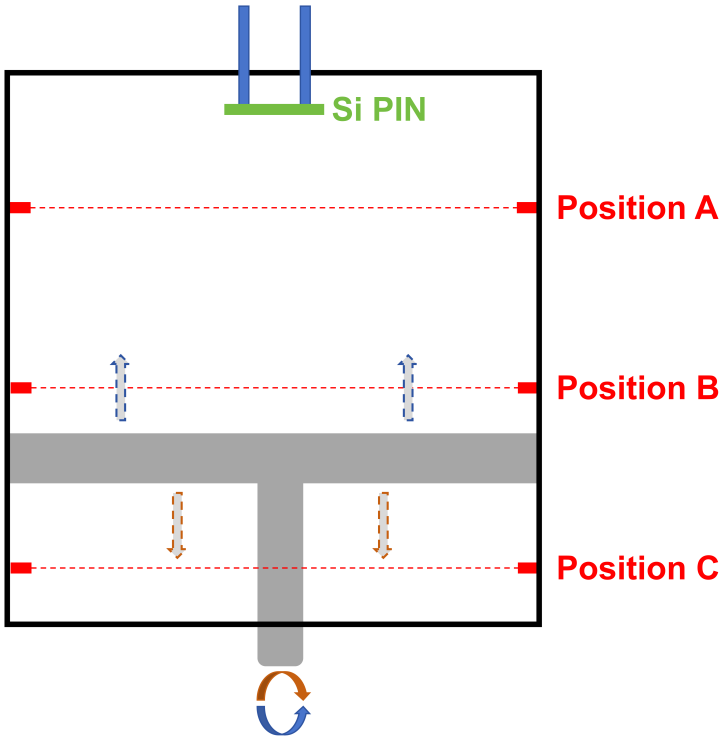

Figure 5–1 The figure shows a possible radon measurement system chamber design with multiple selectable volume positions. The red dashed lines indicate the three selectable volume positions. The gray shape represents a movable stainless steel piston that serves as the bottom of each volume position.

Inspired by syringe-like designs, Figure 5–1 illustrates a possible new detector chamber for a radon measurement system. The gray shape in the figure represents a stainless steel

piston that can be adjusted up and down to switch between different volume positions (A, B, and C), depending on the sample size. For smaller samples, selecting a lower volume position improves radon progeny collection efficiency while reducing the chamber's inner surface exposure to air, thereby minimizing the chamber's radon emission rate. To further reduce the detector's radon background, radon-blocking membranes or low-background coatings could be applied to the piston's surfaces and the chamber's interior.

5.3 Online Radon Removal by Centrifugal Separation

In various low background experiments, radon diffusion from detector construction materials into the sensitive area during data-taking is a persistent challenge. To address this, many experiments have devised online radon removal systems, with cryogenic distillation being a commonly used method[66]. This technique uses a cryogenic distillation column to collect and purify gaseous xenon in the detector to remove trace amounts of radon. While this method can eliminate some radon, the remaining amount requires further solutions. Figure 5–2 illustrates a potential approach for the future. This discussion focuses only on the physical feasibility of the strategy, leaving technical and more complex engineering issues for later consideration.

Since both ^{222}Rn and ^{220}Rn are significantly heavier than xenon and its isotopes, we can consider high-speed centrifugal separation to remove these backgrounds. In this method, the TPC functions similarly to a washing machine drum. During experimental pauses or before data collection, high-speed centrifugation of the liquid xenon inside the TPC can separate heavier atoms, which experience greater centrifugal forces and thus are pushed outward. This results in the outer layer of liquid xenon containing more high-mass radioactive impurities.

To enhance the effectiveness of background reduction, this method aims to minimize the introduction of additional materials into the TPC. The red circles in the diagram represent an annular heating band mounted on the Teflon exterior, which heats the upper layer of xenon gas. As the gas expands from heating, the pressure on the liquid xenon below increases, facilitating the control of the subsequent discharge process for the high-impurity liquid xenon. The internal geometry of the Teflon vessel holding the liquid xenon is redesigned to feature a continuous grooved surface instead of a smooth plane. These grooves connect to drainage pipes to control the discharge of the liquid xenon. This way, the outer layer of liquid xenon,

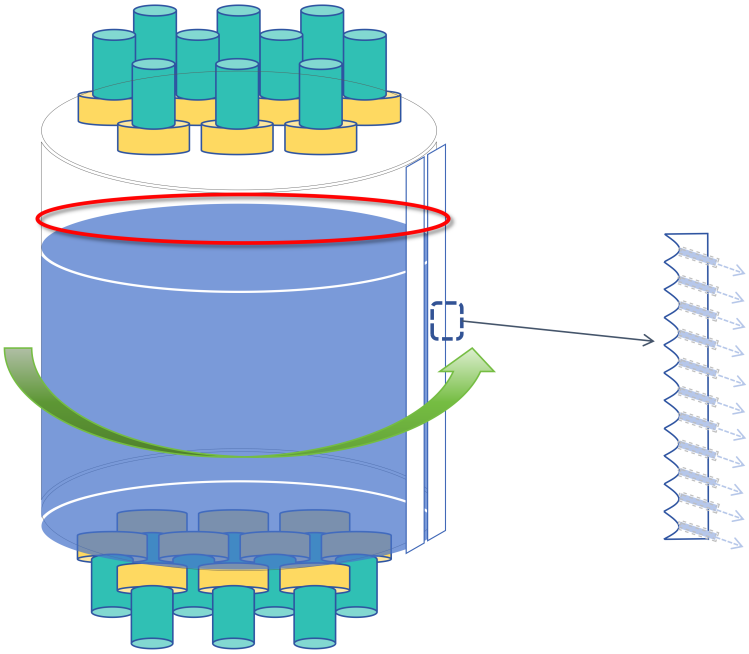

Figure 5–2 The figure shows a simplified diagram of TPC modification for online radon removal using centrifugal separation (with LXe TPC as an example). The red circles represent heating bands used to heat the xenon gas to pressurize the detector. The dashed rectangle shows the new geometry of Teflon, featuring a continuous grooved surface and an outlet pipe for draining liquid xenon enriched with impurities

containing more radon after centrifugation, is collected, vaporized, and subjected to a series of radon removal processes before being recirculated into the TPC as purer xenon gas. Indeed, changes to Teflon's surface geometry could impact the photon collection efficiency during experiments. This might necessitate employing improved manufacturing techniques to achieve Teflon surfaces with higher reflectivity or alternatively adopting other methods to compensate for any potential losses in efficiency.

Since this method is sensitive only to the atomic mass number, other heavy elements besides radon are also expected to be flung outward along with radon. However, several issues require further investigation. For example, will the increased surface area of the Teflon lead to more background contamination? How can we effectively control the high-speed centrifugation of tons or even tens of tons of liquid xenon? How can gas pressurization efficiently discharge radioactive impurity-rich liquid xenon from different levels? If this method is considered for use in the future for radon removal, these issues must be addressed and resolved.

5.4 Summary

In this chapter, we explored several innovative strategies and methods for radon control and measurement in low background experiments. We started by proposing that our radon diffusion chamber could measure radon solubility constants in membrane materials. With some adjustments to the experimental setup and design of the chamber, this system can yield more accurate measurements, improving our ability to select materials with a better radon-blocking effect.

We then discussed methods to reduce the inherent background levels in radon measurement systems. By applying surface treatments or radon-blocking membranes to detector chambers, we can expect lower radon emissions, allowing the accurate detection of materials with extremely low radon emanation rates. We also discussed the radon measurement system chamber's design with multiple selectable volumes here.

Ultimately, we introduced a concept for online radon removal using high-speed centrifugal separation. This approach takes advantage of the mass difference between radon and xenon to separate radon atoms from liquid xenon in the Time Projection Chamber. While promising, it requires further exploration to address engineering and practical challenges.

Together, these strategies could provide valuable insights into future radon control and measurement techniques, paving the way for improved radon-sensitive experiments.

Chapter 6 Summary

In this comprehensive exploration of the hidden universe, we delved into the enigmatic realms of dark matter and neutrinos, as well as the challenges associated with their detection. These low background experiments, often located deep underground, might hold the key to unlocking unknown physics. Controlling background noise is crucial to their success. This thesis specifically examines radon-related measurement and control techniques in these low background experiments.

Currently, rare event detection experiments in the fields of dark matter and neutrinos are flourishing worldwide, with intense international competition. In dark matter research, the LZ experiment and DarkSide-20k experiment focus primarily on WIMPs, while the Axion Dark Matter experiment (ADMX) and SuperCDMS experiment aim to search for lighter dark matter models like axions. Large-scale facilities such as the LHC and the future IceCube-G2 could also play a significant role in uncovering the nature of dark matter. Astrophysical projects like CMB-S4 and the Southern Wide-field Gamma-ray Observatory (SWGO) will provide critical information to support dark matter detectors. Naturally, these large-scale experiments involve different background control logic than the deep underground low background experiments. In neutrino research, the nEXO and JUNO experiments will offer improved results in measuring the neutrino mass hierarchy and searching for neutrinoless double-beta decay. Similar efforts are underway with experiments like NOvA and DUNE in the U.S. and Japan's T2K experiments. We hope that one of these experiments will lead us to discover new and intriguing physics. For most of them, managing the background levels will be crucial for achieving their goals.

For most low background experiments, radon is a pervasive and troublesome issue. Its decay products can create false signals in detectors, potentially drowning out the actual target signals. This thesis extensively discusses the background effects caused by radon in detectors and techniques for controlling and measuring radon levels in experimental materials. These methods have long been used effectively in particle physics experiments. With ongoing improvements in detector capabilities and the development of new techniques, we should expect that increasingly low-radon-background environments will be achieved.

However, there are some points I believe experimenters should reflect upon. With significant resources and effort now devoted to low background experiments, we seem to be too focused on existing approaches. In TPC-based experiments, successive generations of detectors have been upgraded, increasing the amount of target material from kilograms to tens of tons, while reducing various types of background. Everything appears to be moving in the right direction. However, if the next generation of experiments still can't provide satisfactory answers, will we continue to build even larger detectors with even lower background levels? While upgrading from one generation to the next certainly has its advantages, as it promotes technical innovation, we may be losing our initial instinct for fundamental physics.

Similar to the gravitational wave detection experiments from decades ago, the resonant aluminum bar detectors[67] were pioneering in gravitational wave detection. Subsequently, there was a solid effort to lower temperatures to increasingly colder levels and better control background noise. Despite these efforts, no convincing experimental evidence was found. Instead, the novel approach later adopted by the LIGO experiment, which utilized a Michelson interferometer-based detector, first successfully detected gravitational waves[68]. This success certainly involved an element of luck, but it undoubtedly represents a triumphant experience in the search for rare signals in physics. We sincerely hope the next generation of experiments will yield groundbreaking results. Still, if not, we would like to see more funding and ingenuity invested in exploring new ideas and experimental techniques, which could be a better future for both fundamental physics and detector technology.

Bibliography

[1] BURGESS C P, MOORE G D. The standard model: A primer[M]. Cambridge University Press, 2006.

[2] DOMINGUEZ D. Particles of the Standard Model of particle physics[Z]. https://home.cern/science/physics/standard-model. [Accessed 20-05-2024]. 2024.

[3] HAO-ZHE Z, YUAN-YUAN L, LI W, et al. Application and development of liquid argon detector in rare event detection[J]. Acta Phys. Sin., 2023, 72: 100-113.

[4] Planck Collaboration, AGHANIM N, AKRAMI Y, et al. Planck 2018 results. VI. Cosmological parameters[J]., 2020, 641, A6: A6. arXiv: 1807.06209 [astro-ph.CO]. DOI: 10.1051/0004-6361/201833910.

[5] VOLDERS L. Neutral hydrogen in M 33 and M 101[J/OL]. Bulletin of the Astronomical Institutes of the Netherlands, (1959-09-01)[2024-06-03], 14: 323. https://api.semanticscholar.org/CorpusID:93909378.

[6] RUBIN V C, FORD J, W. K., THONNARD N. Extended rotation curves of high-luminosity spiral galaxies. IV. Systematic dynamical properties, Sa -> Sc.[J]., 1978, 225: L107-L111. DOI: 10.1086/182804.

[7] Planck Collaboration, ADE P A R, AGHANIM N, et al. Planck 2015 results. XIII. Cosmological parameters[J]., 2016, 594, A13: A13. arXiv: 1502.01589 [astro-ph.CO]. DOI: 10.1051/0004-6361/201525830.

[8] BALTZ E A. Dark matter candidates[J]. eConf, 2004, C040802: L002. arXiv: astro-ph/0412170.

[9] BATTAGLIERI M, BELLONI A, CHOU A, et al. US Cosmic Visions: New Ideas in Dark Matter 2017: Community Report[Z]. 2017. arXiv: 1707.04591 [hep-ph].

[10] BILAL A. Introduction to supersymmetry[J]. 2001. arXiv: hep-th/0101055.

[11] BAER H, TATA X. Weak scale supersymmetry: From superfields to scattering events[M]. Cambridge University Press, 2006.

[12] GRIEST K, KAMIONKOWSKI M. Supersymmetric dark matter[J]. Phys. Rept., 2000, 333: 167-182. DOI: 10.1016/S0370-1573(00)00021-1.

[13] FENG J L. The WIMP paradigm: Theme and variations[J/OL]. SciPost Phys. Lect. Notes, (2023-06-13)[2024-06-03]: 71. https://scipost.org/10.21468/SciPostPhysLectNotes.71. DOI: 10.21468/SciPostPhysLectNotes.71.

[14] PECCEI R D, QUINN H R. CP Conservation in the Presence of Instantons[J]. Phys. Rev. Lett., 1977, 38: 1440-1443. DOI: 10.1103/PhysRevLett.38.1440.

[15] WILCZEK F. Problem of Strong P and T Invariance in the Presence of Instantons[J]. Phys. Rev. Lett., 1978, 40: 279-282. DOI: 10.1103/PhysRevLett.40.279.

[16] GEORGI H, GLASHOW S L. Unity of All Elementary Particle Forces[J]. Phys. Rev. Lett., 1974, 32: 438-441. DOI: 10.1103/PhysRevLett.32.438.

[17] MOHAPATRA R N, SENJANOVI Ć G. Neutrino Mass and Spontaneous Parity Nonconservation [J/OL]. Phys. Rev. Lett., (1980-04-07)[2024-06-03], 44: 912-915. https://link.aps.org/doi/10.1103/PhysRevLett.44.912. DOI: 10.1103/PhysRevLett.44.912.

[18] REINES F, COWAN C L. A Proposed Experiment to Detect the Free Neutrino[J/OL]. Phys. Rev., (1953-05-01)[2024-06-03], 90: 492-493. https://link.aps.org/doi/10.1103/PhysRev.90.492.2. DOI: 10.1103/PhysRev.90.492.2.

[19] REINES F, COWAN C L. Detection of the Free Neutrino[J/OL]. Phys. Rev., (1953-11-01)[2024-06-03], 92: 830-831. https://link.aps.org/doi/10.1103/PhysRev.92.830. DOI: 10.1103/PhysRev.92.830.

[20] DANBY G, GAILLARD J M, GOULIANOS K, et al. Observation of High-Energy Neutrino Reactions and the Existence of Two Kinds of Neutrinos[J/OL]. Phys. Rev. Lett., (1962-07-01)[2024-06-03], 9: 36-44. https://link.aps.org/doi/10.1103/PhysRevLett.9.36. DOI: 10.1103/PhysRevLett.9.36.

[21] KODAMA K, USHIDA N, ANDREOPOULOS C, et al. Observation of tau neutrino interactions [J/OL]. Physics Letters B, (2001-04-12)[2024-06-03], 504(3): 218-224. https://www.sciencedirect.com/science/article/pii/S0370269301003070. DOI: https://doi.org/10.1016/S0370-2693(01)00307-0.

[22] DAVIS R, HARMER D S, HOFFMAN K C. Search for Neutrinos from the Sun[J/OL]. Phys. Rev. Lett., (1968-05-20)[2024-06-03], 20: 1205-1209. https://link.aps.org/doi/10.1103/PhysRevLett.20.1205. DOI: 10.1103/PhysRevLett.20.1205.

[23] BAHCALL J N, BAHCALL N A, SHAVIV G. Present status of the theoretical predictions for the Cl-36 solar neutrino experiment[J]. Phys. Rev. Lett., 1968, 20: 1209-1212. DOI: 10.1103/PhysRevLett.20.1209.

[24] GRIBOV V, PONTECORVO B. Neutrino astronomy and lepton charge[J/OL]. Physics Letters B, (1969-01-20)[2024-06-03], 28(7): 493-496. https://www.sciencedirect.com/science/article/pii/0370269369905255. DOI: https://doi.org/10.1016/0370-2693(69)90525-5.

[25] FUKUDA S, et al. Solar B-8 and hep neutrino measurements from 1258 days of Super-Kamiokande data[J]. Phys. Rev. Lett., 2001, 86: 5651-5655. arXiv: hep-ex/0103032. DOI: 10.1103/PhysRevLett.86.5651.

[26] AHMAD Q R, ALLEN R C, ANDERSEN T C, et al. Measurement of the Rate of $\nu_e + d \rightarrow p + p + e^-$ Interactions Produced by ^8B Solar Neutrinos at the Sudbury Neutrino Observatory[J/OL]. Phys. Rev. Lett., (2001-07-25)[2024-06-03], 87: 071301. https://link.aps.org/doi/10.1103/PhysRevLett.87.071301. DOI: 10.1103/PhysRevLett.87.071301.

[27] AHMAD Q R, ALLEN R C, ANDERSEN T C, et al. Direct Evidence for Neutrino Flavor Transformation from Neutral-Current Interactions in the Sudbury Neutrino Observatory[J/OL]. Phys. Rev. Lett., (2002-06-13)[2024-06-03], 89: 011301. https://link.aps.org/doi/10.1103/PhysRevLett.89.011301. DOI: 10.1103/PhysRevLett.89.011301.

[28] BETTINI A. Introduction to Elementary Particle Physics[M]. 2nd ed. Cambridge University Press, 2014.

[29] FORMAGGIO J A, DE GOUVÊA A L C, ROBERTSON R H. Direct measurements of neutrino mass[J/OL]. Physics Reports, (2021-06-03)[2024-06-03], 914: 1-54. https://www.sciencedirect.com/science/article/pii/S0370157321000636. DOI: https://doi.org/10.1016/j.physrep.2021.02.002.

[30] ADAMS D, ALDUINO C, ALFONSO K, et al. CUORE: The first bolometric experiment at the ton scale for rare decay searches[J/OL]. Nuclear Instruments and Methods in Physics Research Section A: Accelerators, Spectrometers, Detectors and Associated Equipment, (2019-08-21)[2024-06-03], 936: 158-161. https://www.sciencedirect.com/science/article/pii/S0168900218316826. DOI: https://doi.org/10.1016/j.nima.2018.11.073.

[31] AKERIB D S, ALSUM S, ARAÚJO H M, et al. Results from a Search for Dark Matter in the Complete LUX Exposure[J/OL]. Phys. Rev. Lett., (2017-01-11)[2024-06-03], 118: 021303. https://link.aps.org/doi/10.1103/PhysRevLett.118.021303. DOI: 10.1103/PhysRevLett.118.021303.

[32] AKIMOV D, ARAÚJO H, BARNES E, et al. WIMP-nucleon cross-section results from the second

science run of ZEPLIN-III[J/OL]. Physics Letters B, (2012-03-13)[2024-06-03], 709(1): 14-20. https://www.sciencedirect.com/science/article/pii/S0370269312001050. DOI: https://doi.org/10.1016/j.physletb.2012.01.064.

[33] MOUNT B J, HANS S, ROSERO R, et al. LUX-ZEPLIN (LZ) Technical Design Report[Z]. 2017. arXiv: 1703.09144 [physics.ins-det].

[34] COLLABORATION T L, AKERIB D S, AKERLOF C W, et al. LUX-ZEPLIN (LZ) Conceptual Design Report[Z]. 2015. arXiv: 1509.02910 [physics.ins-det].

[35] AKERIB D S, AKERLOF C W, ALSUM S K, et al. Projected WIMP sensitivity of the LUX-ZEPLIN dark matter experiment[J/OL]. Phys. Rev. D, (2020-03-04)[2024-06-03], 101: 052002. https://link.aps.org/doi/10.1103/PhysRevD.101.052002. DOI: 10.1103/PhysRevD.101.052002.

[36] AKERIB D, AKERLOF C, AKIMOV D, et al. The LUX-ZEPLIN (LZ) experiment[J/OL]. Nuclear Instruments and Methods in Physics Research Section A: Accelerators, Spectrometers, Detectors and Associated Equipment, (2020-02-11)[2024-06-03], 953: 163047. https://www.sciencedirect.com/science/article/pii/S0168900219314032. DOI: https://doi.org/10.1016/j.nima.2019.163047.

[37] XIAO M, et al. First dark matter search results from the PandaX-I experiment[J]. Sci. China Phys. Mech. Astron., 2014, 57: 2024-2030. arXiv: 1408.5114 [hep-ex]. DOI: 10.1007/s11433-014-5598-7.

[38] CUI X, ABDUKERIM A, CHEN W, et al. Dark Matter Results from 54-Ton-Day Exposure of PandaX-II Experiment[J/OL]. Phys. Rev. Lett., (2017-10-30)[2024-06-03], 119: 181302. https://link.aps.org/doi/10.1103/PhysRevLett.119.181302. DOI: 10.1103/PhysRevLett.119.181302.

[39] MENG Y, et al. Dark Matter Search Results from the PandaX-4T Commissioning Run[J]. Phys. Rev. Lett., 2021, 127(26): 261802. arXiv: 2107.13438 [hep-ex]. DOI: 10.1103/PhysRevLett.127.261802.

[40] ZHANG H, et al. Dark matter direct search sensitivity of the PandaX-4T experiment[J]. Sci. China Phys. Mech. Astron., 2019, 62(3): 31011. arXiv: 1806.02229 [physics.ins-det]. DOI: 10.1007/s11433-018-9259-0.

[41] AALSETH C E, et al. DarkSide-20k: A 20 tonne two-phase LAr TPC for direct dark matter detection at LNGS[J]. Eur. Phys. J. Plus, 2018, 133: 131. arXiv: 1707.08145 [physics.ins-det]. DOI: 10.1140/epjp/i2018-11973-4.

[42] ADAM T, AN F, AN G, et al. JUNO Conceptual Design Report[Z]. 2015. arXiv: 1508.07166 [physics.ins-det].

[43] AN F, AN G, AN Q, et al. Neutrino physics with JUNO[J/OL]. Journal of Physics G: Nuclear and Particle Physics, (2016-02-10)[2024-06-03], 43(3): 030401. https://dx.doi.org/10.1088/0954-3899/43/3/030401. DOI: 10.1088/0954-3899/43/3/030401.

[44] JUNO physics and detector[J/OL]. Progress in Particle and Nuclear Physics, (2022-12-03)[2024-06-03], 123: 103927. https://www.sciencedirect.com/science/article/pii/S0146641021000880. DOI: https://doi.org/10.1016/j.ppnp.2021.103927.

[45] KHARUSI S A, et al. nEXO Pre-Conceptual Design Report[J]. 2018. arXiv: 1805.11142 [physics.ins-det].

[46] JEWELL M J. Search for neutrinoless double beta decay with EXO-200 and nEXO[D]. Stanford U., 2020.

[47] SI L. Ultra low background control technique and determination of double beta decay half-life of ^{136}Xe[D]. Shanghai Jiao Tong U., 2023.

[48] KUDRYAVTSEV V, ZAKHARY P, EASEMAN B. Neutron production in (α,n) reactions[J/OL].

Nuclear Instruments and Methods in Physics Research Section A: Accelerators, Spectrometers, Detectors and Associated Equipment, (2020-08-21)[2024-06-03], 972: 164095. https://www.sciencedirect.com/science/article/pii/S0168900220305088. DOI: https://doi.org/10.1016/j.nima.2020.164095.

[49] AALBERS J, et al. Background determination for the LUX-ZEPLIN dark matter experiment[J]. Phys. Rev. D, 2023, 108(1): 012010. arXiv: 2211.17120 [hep-ex]. DOI: 10.1103/PhysRevD.108.012010.

[50] JEREMIE A. The SuperNEMO demonstrator double beta experiment[J/OL]. Nuclear Instruments and Methods in Physics Research Section A: Accelerators, Spectrometers, Detectors and Associated Equipment, (2020-04-01)[2024-06-03], 958: 162115. https://www.sciencedirect.com/science/article/pii/S0168900219305431. DOI: https://doi.org/10.1016/j.nima.2019.04.069.

[51] MOTT J. Search for double beta decay of ^{82}Se with the NEMO-3 detector and development of apparatus for low-level radon measurements for the SuperNEMO experiment[D]. U. Coll. London, 2013.

[52] PAGELKOPF P, PORSTENDÖRFER J. Neutralisation rate and the fraction of the positive 218Po-clusters in air[J/OL]. Atmospheric Environment, (2003-02-11)[2024-06-03], 37(8): 1057-1064. https://www.sciencedirect.com/science/article/pii/S1352231002009974. DOI: https://doi.org/10.1016/S1352-2310(02)00997-4.

[53] WANG F, WANG H, ZENG Z, et al. A series of high-sensitivity radon detection systems and their applications in nitrogen as well as the boil-off liquid nitrogen measurement[J/OL]. Applied Radiation and Isotopes, (2024-02-28)[2024-06-03], 206: 111260. https://www.sciencedirect.com/science/article/pii/S0969804324000885. DOI: https://doi.org/10.1016/j.apradiso.2024.111260.

[54] ABE K, HIEDA K, HIRAIDE K, et al. Radon removal from gaseous xenon with activated charcoal [J/OL]. Nuclear Instruments and Methods in Physics Research Section A: Accelerators, Spectrometers, Detectors and Associated Equipment, (2012-01-01)[2024-06-03], 661(1): 50-57. https://www.sciencedirect.com/science/article/pii/S0168900211018468. DOI: https://doi.org/10.1016/j.nima.2011.09.051.

[55] PUSHKIN K, AKERLOF C, ANBAJAGANE D, et al. Study of radon reduction in gases for rare event search experiments[J/OL]. Nuclear Instruments and Methods in Physics Research Section A: Accelerators, Spectrometers, Detectors and Associated Equipment, (2018-09-21)[2024-06-03], 903: 267-276. http://dx.doi.org/10.1016/j.nima.2018.06.076. DOI: 10.1016/j.nima.2018.06.076.

[56] MURRA M, SCHULTE D, HUHMANN C, et al. Design, construction and commissioning of a high-flow radon removal system for XENONnT[J]. Eur. Phys. J. C, 2022, 82(12): 1104. arXiv: 2205.11492 [physics.ins-det]. DOI: 10.1140/epjc/s10052-022-11001-9.

[57] DAOUD W, RENKEN K. Laboratory assessment of flexible thin-film membranes as a passive barrier to radon gas diffusion[J/OL]. Science of The Total Environment, (2001-05-14)[2024-06-03], 272(1): 127-135. https://www.sciencedirect.com/science/article/pii/S0048969701006763. DOI: https://doi.org/10.1016/S0048-9697(01)00676-3.

[58] JIRANEK M, SVOBODA Z. Transient radon diffusion through radon-proof membranes: A new technique for more precise determination of the radon diffusion coefficient[J/OL]. Building and Environment, (2009-10-31)[2024-06-03], 44(6): 1318-1327. https://www.sciencedirect.com/science/article/pii/S0360132308002370. DOI: https://doi.org/10.1016/j.buildenv.2008.09.017.

[59] TSAPALOV A, GULABYANTS L, LIVSHITS M, et al. New method and installation for rapid determination of radon diffusion coefficient in various materials[J/OL]. Journal of Environmental Radioactivity, (2014-01-09)[2024-06-03], 130: 7-14. https://www.sciencedirect.com/science/arti

cle/pii/S0265931X13002932. DOI: https://doi.org/10.1016/j.jenvrad.2013.12.010.

[60] QIU S. Calibration of a ^{220}2Rn flow-through source[J/OL]. Radiation and Environmental Biophysics, (2006-08-10)[2024-06-03], 45(1): 215-220. https://link.springer.com/article/10.1007/s00411-006-0059-y#citeas. DOI: https://doi.org/10.1007/s00411-006-0059-y.

[61] UM2606 - DT5780 Dual Digital MCA User Manual rev. 4[A]. CAEN S.p.A., 2016.

[62] Si PIN photodiode S3204/S3584 series[A]. Hamamatsu, 2012.

[63] WOJCIK M. Measurement of radon diffusion and solubility constants in membranes[J/OL]. Nuclear Instruments and Methods in Physics Research Section B: Beam Interactions with Materials and Atoms, (1991-07-02)[2024-06-03], 61(1): 8-11. https://www.sciencedirect.com/science/article/pii/0168583X9195553P. DOI: https://doi.org/10.1016/0168-583X(91)95553-P.

[64] MENG Y, BUSENITZ J, PIEPKE A. A new method for evaluating the effectiveness of plastic packaging against radon penetration[J/OL]. Applied Radiation and Isotopes, (2020-01-30)[2024-06-03], 156: 108963. https://www.sciencedirect.com/science/article/pii/S0969804319302696. DOI: https://doi.org/10.1016/j.apradiso.2019.108963.

[65] RAD7 Electronic Radon Detector User Manual[A]. DURRIDGE Company, 2023.

[66] APRILE E, et al. Online^{222} Rn removal by cryogenic distillation in the XENON100 experiment [J]. Eur. Phys. J. C, 2017, 77(6): 358. arXiv: 1702.06942 [physics.ins-det]. DOI: 10.1140/epjc/s10052-017-4902-x.

[67] WEBER J. Gravitational-Wave-Detector Events[J/OL]. Phys. Rev. Lett., (1968-06-03)[2024-06-03], 20: 1307-1308. https://link.aps.org/doi/10.1103/PhysRevLett.20.1307. DOI: 10.1103/PhysRevLett.20.1307.

[68] ABBOTT B P, ABBOTT R, ABBOTT T D, et al. Observation of Gravitational Waves from a Binary Black Hole Merger[J/OL]. Phys. Rev. Lett., (2016-02-11)[2024-06-03], 116: 061102. https://link.aps.org/doi/10.1103/PhysRevLett.116.061102. DOI: 10.1103/PhysRevLett.116.061102.

List of Research Achievements

[1] S. Yang, L. Wu, Z. Zheng, et al. The stability of unevenly spaced planetary systems[J/OL]. Icarus, 2023, 406:115757, https://www.sciencedirect.com/science/ article/pii/S0019103523003342. DOI: https://doi.org/10.1016/j.icarus.2023.115757.

[2] S. V. Chekanov, S. Eno, S. Magill, et al. Geant4 simulations of sampling and homogeneous hadronic calorimeters with dual readout for future colliders[J]. arXiv:2311.03539 [physics.ins-det].

Acknowledgements

This year marks my third year in experimental high-energy physics, a pure and vibrantly alive discipline. I consider myself extremely fortunate to have been guided into this field during my undergraduate studies, where I have experienced many ups and downs and been supported by many. I want to express my heartfelt shout-out to everyone who deserves credit for their support.

I am particularly grateful to Professor Yue Meng, the first mentor who truly guided me into the world of particle physics research. She is a professional and trusting mentor who began guiding me when I was still a rookie in particle physics, teaching me always to treat my work professionally. She is a truly respected and kind experimental physicist, and I sincerely appreciate her support and sincere advice regarding all my decisions.

I am so fortunate to have had the opportunity to work with Professors Sarah Eno and Christopher Palmer at UMD, which has been a treasured part of my life. Professor Sarah Eno is always willing to dedicate her time to undergraduates and is always ready to provide timely and precise guidance. She is undoubtedly one of the wisest and most experienced high-energy physicists I have ever encountered. Her words, "Ask questions until you understand like a 5-year-old. Ask questions and questions and questions and questions. Real physicists never lose that 5-year-old." profoundly resonated with me. Professor Christopher Palmer's enthusiasm and diligent work have made a lasting impression on me. He is an optimistic and humorous physicist who has taught me much about collider physics. I also greatly appreciate the guidance and help from Yihui Lai, Tim Edberg, Sarah Waldych, Mekhala Mahesh Paranjpe, and Sara Nabili, who supported me and ensured I never felt alone when facing challenges. Thank you all.

I am also extremely grateful to Professor Masahiro Ogihara from Tsung-Dao Lee Institute for his meticulous and efficient work ethic, which has been an excellent example for me. I am thankful for the camaraderie and support of Dr. Kangrou Guo, Sheng Yang, and others during that time. With your help, our research progressed so smoothly.

I truly appreciate having had a peer and slightly older friend during my undergraduate years. Dr. Lin Si has accommodated me with the experimental hardware, especially the

radon system. More importantly, whenever I needed advice before making decisions, she generously shared her experiences and thoughts with me. She was always there when I needed help, inspiring everyone around her with her enthusiastic and optimistic attitude. I hope our friendship continues to endure.

I am also immensely thankful for all my friends in Laboratory 127, Science Building 6 at SJTU. Zhicheng Qian, Youhui Yun, Yuan Wu, Yuan Li, Zhixing Gao, and Hao Wang. Your companionship colored my research days at SJTU, transforming what could have been a monotonous and tense environment into one filled with warmth and humanity.

I am also profoundly grateful to everyone in the PandaX collaboration who has offered help and companionship. A special thanks to Dr. Yi Tao, Xu Wang, Chencheng Han, Zhou Huang, and Xuyang Ning, whose support and presence through different phases have meant a lot to me. Thanks to Professor Ning Zhou for providing me with a workstation in Laboratory 112 and the opportunity to meet all the friends from the TPC group. I sincerely appreciate Professor Ke Han for his repeated guidance and encouragement. His effective mentorship and transparent thought processes have always guided me well. Thanks to Professor Jianglai Liu as well. Although we don't have a direct working relationship, and he might not remember me well, his charismatic persona and professionalism as a particle physicist have long been a benchmark for me, clarifying what kind of scholar I aspire to become.

I am thankful for the peers I met at the School of Physics and Astronomy at SJTU over my undergraduate years. I appreciate classmates like Xinyue Yuan, Zhuowei Zhang and Zijian Li for their patient explanations whenever I encountered course problems. I must also thank my good friends, Rongyi Lv, Congyu Hu, Chenyang Liu, Junde Li, Jasmine Wu, Hanze Guo, and others, in no particular order. Each of you has been a crucial support outside research and a significant part of my undergraduate life. I sincerely thank you all for your companionship and encouragement.

Last but not least, I want to extend my warmest thanks to my family. Thank you to my grandparents and parents for your selfless encouragement and unwavering trust, which have been vital supports for me to move forward boldly with confidence and optimism. Thank you for your understanding and respect for my field of study and for your understanding and selfless support of all my decisions. I cannot repay you enough, but I will continue to channel your love for me into my passion and dedication to physics.